



PCCP

Biexciton dynamics in halide perovskite nanocrystals

Journal:	<i>Physical Chemistry Chemical Physics</i>
Manuscript ID	CP-PER-06-2022-002826.R1
Article Type:	Perspective
Date Submitted by the Author:	15-Aug-2022
Complete List of Authors:	Yumoto, Go; Kyoto University Institute for Chemical Research Kanemitsu, Yoshihiko; Kyoto University Institute for Chemical Research

SCHOLARONE™
Manuscripts

Biexciton dynamics in halide perovskite nanocrystals

Go Yumoto and Yoshihiko Kanemitsu*

Institute for Chemical Research, Kyoto University, Uji, Kyoto 611-0011, Japan

*Correspondence to: kanemitsu@scl.kyoto-u.ac.jp

Abstract

Lead halide perovskite nanocrystals are attracting considerable interest as next-generation optoelectronic materials. Optical responses of nanocrystals are determined by excitons and exciton complexes such as trions and biexcitons. Understanding of their dynamics is indispensable for the optimal design of optoelectronic devices and the development of new functional properties. Here, we summarize the recent advances on the exciton and biexciton photophysics in lead halide perovskite nanocrystals revealed by femtosecond time-resolved spectroscopy and single-dot spectroscopy. We discuss the impact of the biexciton dynamics on controlling and improving the optical gain.

1. Introduction

Currently, halide perovskites described by the formula ABX_3 are receiving much attention as novel semiconductor materials which show intriguing optoelectronic properties from viewpoints of the fundamental physics and optoelectronic device applications.^{1–16} In particular, halide perovskites with the B site occupied by Pb have a stable structure, where organic molecules ($MA = CH_3NH_3$, $FA = HC(NH_2)_2$) or cesium can be used as the A-site cation, and iodine, bromine, and chloride can be used as the X-site halide (Fig. 1a). High-quality thin films and bulk crystals of lead halide perovskites (LHPs) can be simply prepared by solution-based synthesis methods, and actual implementation as light-weight flexible solar cell materials is expected since they also show very high solar-cell conversion efficiencies.^{17–26} The superior solar cell characteristics of LHPs arise from their unique optoelectronic properties such as steep absorption edges, large absorption coefficients, and long diffusion lengths of free carriers.^{27–37} Furthermore, along with the low defect densities within the bandgap, the high photoluminescence (PL) efficiencies and the high transmittance for light with the photon energy below the bandgap^{38–41} suggest that LHPs are one of the promising materials for light-emitting devices and nonlinear optics. In fact, they are attracting much attention for potential applications as high-efficiency light-emitting diodes (LEDs), low-threshold optical gain media, photodetectors, optical modulators, etc.^{42–47}

Low-dimensional nanostructures of LHPs exhibit superior PL properties.^{48–51} In these low-dimensional perovskites, the enhancement of the density of states at the band edge and quantum confinement effects increase the PL efficiency with keeping the excellent optical properties of the three-dimensional bulk crystals. In particular, LHP nanocrystals (NCs), *i.e.* zero-dimensional quantum dots, have been intensively studied since the first report on their synthesis in 2014⁵² and much effort has been devoted to structural characterization and realizing highly efficient PL.^{48,49} Among these studies, it was reported in 2015 that, without a special surface passivation such as a core/shell structure, stable all-inorganic $CsPbX_3$ ($X = Cl, Br, I$) perovskite NCs can be synthesized and they show

extremely high PL quantum yields.⁵³ Moreover, LHP NCs show a well-defined cubic shape and narrow size distribution and exhibit interesting optical properties that differ from those of conventional semiconductor colloidal NCs. For example, LHP NCs naturally form a superlattice structure when the solvent is evaporated, which was reported to show superfluorescence.⁵⁴

Halide substitution and control of the NC size and shape make it possible to tune the bandgap energy of LHP NCs over the entire visible region.^{53,55-57} In addition to such good tunability of the bandgap, their low defect density in the bandgap and high PL quantum yields make LHP NCs promising for potential applications as LEDs, lasers, etc.⁵⁸⁻⁶⁰ A large optical gain is expected to occur due to the quantum confinement of carriers in NCs. In fact, it has been observed in CsPbX₃ NCs that light amplification with a low threshold occurs in the entire visible region.⁶⁰ As shown in Fig. 1b, in such nonlinear optical responses, not only excitons (which are pairs of an electron and a hole), but also exciton complexes such as charged excitons (or trions, which are states where one electron or one hole is added to an exciton) and biexcitons (which are bound states consisting of two excitons) are formed.⁶¹⁻⁶⁴ Because LHP NCs are ionic crystals, trions play an important role in optical responses.⁶¹

It is known that, if biexcitons and multiexcitons exist in a semiconductor NC, the optical gain is strongly influenced by exciton many-body effects.⁶²⁻⁶⁸ Due to their band structure characteristics, the influence of exciton–exciton interactions on the optical responses is especially important in the LHP NCs.^{69,70} In particular, because the biexciton dynamics determines the lifetime of the optical gain, its detailed understanding is important with respect to the development of optimal laser designs and optical-gain switching devices.⁷⁰⁻⁷⁴ The biexciton generation and relaxation dynamics are also inevitable for the understanding of many-body effects such as multiple exciton generation (MEG) and Auger recombination processes. Efficient MEG is induced by single-photon excitation in nanomaterials such as NCs, carbon nanotubes, and coupled NC films.⁷⁵⁻⁸³ The MEG and Auger recombination processes in NCs are shown in Fig. 1c. Photoexcitation with a photon energy much larger than the bandgap energy generates an electron and a hole, which possess a large excess energy. An electron-hole pair with such large excess energy creates another electron-hole pair through the MEG process. The Auger recombination process is a non-radiative process where the electron–hole recombination energy is not emitted as a photon, but is transferred to another electron or hole.⁸⁴ The MEG process is important in terms of improving the performance of solar cells and photodetectors.^{85,86} The Auger process plays a key role in understanding the blinking phenomenon in NCs⁸⁷⁻⁸⁹ and the efficiency reduction of LEDs under high voltages, *i.e.* the droop phenomenon.^{90,91} Colloidal NCs are also known to serve as a single photon emitter.^{92,93} A biexciton emits a single photon in single NCs when a biexciton relaxes to the exciton state via a non-radiative Auger recombination process. It has been reported that LHP NCs exhibit excellent properties as room-temperature single-photon sources,^{94,95} which also shows the importance of biexciton dynamics in LHP NCs.

In this Perspective, we provide a summary of recent advances on biexciton dynamics in LHP NCs. We highlight that the exciton–exciton interactions play an important role in the optical responses and especially in the optical gain characteristics of LHP NCs. First, in Section 2 we describe the electronic states of LHPs, which are revealed by nonlinear optical measurements. Then, in Section 3 we discuss the exciton and biexciton dynamics in LHP NCs measured by femtosecond transient absorption spectroscopy, time-resolved PL spectroscopy, and single-dot spectroscopy. In Section 4 we show that the many-body interactions between excitons significantly

impact the optical properties of LHP NCs, and that the biexciton is important in controlling and improving the optical gain characteristics. Finally, in Section 5 we present conclusions and perspectives.

2. Band-edge structure of lead halide perovskite semiconductors

The electronic states of APbX_3 consist of conduction-band states that are mainly composed of the Pb $6p$ orbitals and valence-band states that are characterized by the Pb $6s$ orbital (Fig. 2a).⁹⁶ Furthermore, the large spin-orbit interaction resulted from the presence of the heavy Pb atom splits the conduction-band states into low- and high-energy states, which are separated by the spin-orbit splitting energy Δ_{so} .⁹⁷ The split-off states with the total angular momentum $J = 1/2$ ($|\pm 1/2\rangle^{\text{so}}$) are formed at the band edge while the heavy- and light-electron states with $J = 3/2$ ($|\pm 3/2\rangle^{\text{he}}$ and $|\pm 1/2\rangle^{\text{le}}$, respectively) appear at higher energies. Here, $|m\rangle$ denotes the electronic state with a total electron angular momentum projection along the light propagation direction of m . In Fig. 2b, we show the energy diagram of the electronic states and the optical selection rules.^{97–100} The electronic states at the band edge of APbX_3 can be described by rather simple doubly degenerate states for both the conduction band and the valence band: the valence- and conduction-band states with $J = 1/2$ ($|\pm 1/2\rangle^{\text{v}}$ and $|\pm 1/2\rangle^{\text{so}}$, respectively). Due to these band-edge states, the band-edge optical responses are characterized to be circular polarization dependent optical transitions.^{98,101}

Nonlinear optical measurements are an effective method to reveal this band structure.^{101–104} Two-photon absorption (TPA) is the third-order nonlinear optical effect where excitation light with photon energy E_{ex} generates photoexcited carriers with an energy of $2E_{\text{ex}}$. The excitation-energy dependence of the TPA coefficient β of an MAPbBr_3 single crystal is shown in the top panel of Fig. 2c.¹⁰⁴ While β gently increases for two-photon energies $2E_{\text{ex}}$ from 2.3 to 3.2 eV, a steep increase appears as $2E_{\text{ex}}$ exceeds 3.2 eV. The value of 2.3 eV, where the onset of TPA is observed, corresponds to the bandgap energy of MAPbBr_3 . On the other hand, the steep increase starting from 3.2 eV reflects the contribution from the high-energy states of the conduction band (Fig. 2a). This is clearly seen from the excitation-energy dependence of the TPA dichroism (Fig. 2c, bottom panel). The TPA dichroism can be obtained by measuring β for linearly and circularly polarized excitation lights. From the local minimum in the TPA dichroism, a spin-orbit splitting energy Δ_{so} is estimated to be 0.8 eV. In wide-gap perovskites, exciton effects play an essential role in optical spectra even at room temperature.^{102,103}

The multi-level electronic structure originating from a large spin-orbit interaction has also been revealed by optical Stark spectroscopy of CsPbBr_3 NCs.¹⁰¹ As shown in Fig. 2b, the band-edge optical responses of LHP NCs are determined by optical transitions from $|-1/2\rangle^{\text{v}}$ to $|+1/2\rangle^{\text{so}}$ and from $|+1/2\rangle^{\text{v}}$ to $|-1/2\rangle^{\text{so}}$, which can be excited by right- (σ^+) and left- (σ^-) handed circularly polarized lights, respectively. In the exciton picture, the σ^+ - and σ^- -active optical transitions correspond to the excitation of the excitons with total exciton angular momentum projections of $J_{\text{ex}} = +1$ and -1 , respectively. Consequently, when σ^+ (σ^-)-laser light with a photon energy of $\hbar\omega < E_0$ (E_0 : the exciton energy) irradiates LHP NCs, the exciton energy of $|+1\rangle^{\text{ex}}$ ($|-1\rangle^{\text{ex}}$) shifts from E_0 to $E_0 + \delta E$ only during the laser excitation. This ultrafast energy shift is called the optical Stark effect (Fig. 2d).^{105–109} Figure 2e shows the pump energy dependence of the energy shift of $|+1\rangle^{\text{ex}}$ in CsPbBr_3 NCs, which was observed in pump-probe measurements with σ^+ -pump and σ^+ -probe pulses.¹⁰¹ In the visible excitation region, the energy shift decreases with decreasing pump-photon energies, which can be explained by the optical Stark effect in two-level systems (Fig. 2e, black curve). On the other hand, when the pump-photon energy is reduced further and is in near-infrared region, the energy shift starts to increase. This behavior is in contrast to that expected for the optical Stark effect in two-level

systems (Fig. 2e, red curve).¹⁰¹ It has been revealed that the origin of the energy shift enhancement in the near-infrared region is the Autler–Townes effect¹⁰⁵ resulting from the interaction between light and a multi-level electronic system.

The nonlinear optical measurements have revealed the electronic structure as shown in Fig. 2a and the spin–orbit splitting energy. The doubly degenerate conduction- and valence-band edge states show that at most two electrons and two holes can be excited in a LHP NC. Therefore, the band-edge optical responses of LHP NCs can be determined by excitons, trions, and biexcitons. Since the excitation of the biexciton state reflects the optical selection rules for excitons, a selective excitation is possible by using circularly polarized laser light.⁷³ Hence, polarization-resolved spectroscopy is an effective method for understanding the biexciton state (Fig. 2f). The low degeneracy of the band-edge states means that population inversion occurs at low excitation intensities. This shows that compared to conventional inorganic semiconductor NCs, LHP NCs are promising materials for low-threshold optical-gain media.¹¹⁰ Moreover, the absence of higher-order multiexcitons such as triexcitons (which are generated if three excitons form a bound state) shows that LHP NCs have great potential for application in single-photon sources.^{94,111}

Inversion symmetry breaking and strong spin–orbit interaction bring about unique spin-split electronic states in solids. The spin splitting without external magnetic field is called Rashba splitting.^{112,113} Because the Rashba spin–orbit interaction can be considered as an effective magnetic field depending on the momentum of the electron k , the interaction induces the spin splitting whose energy spacing is determined by k . Due to the strong spin–orbit interactions in LHPs, there has been an active discussion on whether the Rashba splitting modifies the energy structure near the band edge (Fig. 3a).^{114–118} In solids with Rashba-split band structure, circular photogalvanic effect occurs, where the photocurrent can be generated without electric field and the direction of the photocurrent is reversed depending on whether the excitation light is right- or left-handed circularly polarized. In LHPs, the circular photogalvanic effect has been reported.¹¹⁵

The Rashba effect has been reported to play an important role in determining the electronic states of LHP NCs. As shown in Fig. 3b,¹¹⁹ the energies of the bright exciton states with a total exciton angular momentum of $J = 1$ can become lower than that of the dark exciton state with $J = 0$ due to the Rashba effect. Since the energy shift is a few meV, the influence of the Rashba effect has intensively studied in the exciton dynamics at low temperatures.^{100,120} The exciton recombination lifetimes in CsPbX₃ NCs at low temperatures have been observed to be very short ($< \sim 100$ ps) compared to the recombination lifetimes of other inorganic semiconductor NCs.¹⁰⁰ In contrast, it has been experimentally reported that the lowest state in FAPbX₃ NCs is dark, like in conventional semiconductor NCs.^{120,121} The question whether or not the lowest energy level of LHP NCs changes by the Rashba effect should be solved, and further thorough investigations, *e.g.* on the role of the organic molecule at low temperatures, are needed. The understanding of the exciton fine structures^{122–124} and the lowest electronic level^{100,120,121} is particularly important for the development of quantum light sources based on LHP NCs.

One of characteristics of NCs is the size-dependent bandgap energy.^{125–127} So far, investigations on the quantum confinement effects in the semiconductor NCs have been focused on NCs with an almost spherical shape. For example, CdSe NCs with a strong confinement (individual confinement)^{128,129} and CuCl NCs with a weak confinement (exciton confinement)^{130,131} have been studied, and the size confinement effect on the optical properties has been clarified. On the other hand, the LHP NCs are different from these conventional inorganic semiconductor NCs: they have a cubic shape and their size is relatively large. In ref. 132, the size effect in LHP

NCs with an intermediate confinement was calculated and discussed in detail. As shown in Fig. 3c, these calculations well reproduce the experimentally obtained size dependence of the absorption band edge energy of LHP NCs, where the experimental data are taken from refs. 53, 133, and 134. In addition, LHP NCs with higher photo and water stability have recently been explored, and one of them is the structure consisting of CsPbBr₃ NCs embedded in a Cs₄PbBr₆ crystal.¹³⁵⁻¹³⁷ Its green PL is emitted with a high efficiency of more than 90% and is very stable compared to bare colloidal CsPbBr₃ NCs (Fig. 3d).¹³⁷ Below we review the biexciton photophysics of cubic-shaped LHP NCs synthesized by colloidal methods.

3. Recombination dynamics in lead halide perovskite nanocrystals

3.1 Biexciton recombination dynamics

The ultrafast dynamics of excitons, trions, and biexcitons in LHP NCs can be investigated in detail by using femtosecond transient absorption spectroscopy and time-resolved PL spectroscopy.^{61,69-74,138-144} In transient absorption spectroscopy, excitons, trions, and biexcitons generated by a pump pulse can be measured via the change in the transmission of a probe pulse. The transient absorption measurements can probe the dynamics in the time scale typically ranging from the femtoseconds (on the order of the laser pulse width) to nanoseconds. The NCs dispersed solution samples are usually used and samples are stirred with a magnetic stirrer during the transient absorption measurements to avoid sample degradation. Monitoring the absorption spectra of the NCs after the measurements can confirm that the samples are not degraded. As shown in Fig. 4a, the transmission of the probe pulse with photon energies around the band edge depends on the number of electrons and holes excited in the NC. The temporal change of this number is mainly determined by non-radiative Auger recombination and radiative recombination, and their time constants also strongly differ for excitons, trions, and biexcitons.

In Fig. 4b, we show typical examples of the dynamics of the pump-induced change in transmission $\Delta T/T$ in LHP NCs, which were measured in CsPbBr₃ NCs (an average edge length of 7.6 nm) using the pump pulses with a photon energy of 2.82 eV and the probe pulses with photon energies around the band-edge exciton energy of 2.44 eV.^{139,142} When the pump photon fluence j is small, $\Delta T/T$ decays with a single exponential function that has relaxation lifetime on the nanosecond time scale. On the other hand, as j is increased, fast decay components appear and the dynamics can be reproduced using triple exponential functions, which represent the exciton, trion, and biexciton components. By fitting to the dynamics of $\Delta T/T$ for different j with the triple exponential functions, the lifetimes of the exciton (τ_X), trion (τ_{X^+}), and biexciton (τ_{XX}) can be estimated to be 5.1 ns, 280 ps, and 52 ps, respectively.¹⁴² In addition to the lifetimes, the j dependence of the amplitudes of the exciton (A_X), trion (A_{X^+}), and biexciton (A_{XX}) can be obtained (Fig. 4c). The j dependence of A_X can be explained by considering that the generation probability of excitons in a NC is described by the Poisson distribution.^{62,138,139} In order to generate an exciton, it is necessary that one or more photons are absorbed by a NC. Therefore, using the Poisson distribution, the exciton generation probability P_X is given by $1 - e^{-\langle N \rangle}$. Here, the average number of absorbed photons per NC, $\langle N \rangle$, is written as $\langle N \rangle = j\sigma$, where σ is the NC absorption cross-section for the pump photon energy. Because A_X corresponds to the number of excitons generated in a NC, A_X can be well reproduced by $1 - e^{-\langle N \rangle}$ as shown in Fig. 4c. This also shows that τ_X and A_X represent the exciton dynamics. Moreover, by using the value of $\sigma = 1.8 \times 10^{-14}$ cm² estimated from the fitting, we can determine $\langle N \rangle$ as shown in the top axis of Fig. 4c. It can be seen that A_{X^+} and A_{XX} rapidly increase as $\langle N \rangle$ becomes larger.

These results of transient absorption spectroscopy well agree with those of time-resolved PL spectroscopy (Fig. 4d).^{139,140} Under weak excitation conditions $\langle N \rangle \ll 1$, the PL dynamics are determined only by the exciton, which has a long relaxation lifetime on the nanosecond time scale. As $\langle N \rangle$ becomes larger, fast decay components corresponding to the relaxation of trions and biexcitons appear in the PL dynamics immediately after optical excitation. In contrast, the PL dynamics at sufficiently late times after the optical excitation can be described by the exciton with a lifetime of $\tau_X = 5.7$ ns. The data in Fig. 4e are the decay curves for $\langle N \rangle \geq 0.25$ obtained by subtracting the slow decay component of $\tau_X = 5.7$ ns from the PL dynamics. It can be clearly confirmed that two fast decay components appear under strong excitation conditions. The observed fast decay is caused by non-radiative Auger recombination processes.

3.2 Single-dot and single-photon spectroscopy

The above-mentioned transient absorption and time-resolved PL measurements are performed on NC ensembles where NCs are dispersed in a solution. Therefore, the observed results are ensemble averages of the carrier dynamics in NCs with different sizes. Since the lifetimes of trions and biexcitons are expected to exhibit a size dependence, single-dot spectroscopy is a powerful tool for revealing the intrinsic properties of LHP NCs.^{94,95,111,139-141,145} In particular, by measuring the second-order photon correlation $g^{(2)}(t)$ of a single NC, we can clarify the PL and biexciton recombination processes.¹⁴⁶⁻¹⁴⁸ The $g^{(2)}(t)$ function can be obtained by using a Hanbury–Brown–Twiss interferometer (Fig. 5a), where the emission from a single NC is split into two beams and each of them is measured by a single-photon detector. A biexciton can simultaneously emit two photons via the exciton state, and this process is called biexciton–exciton cascade emission (Fig. 5b). A non-zero $g^{(2)}(t)$ at $t = 0$ means the presence of two-photon emission from the biexciton.

In Fig. 5c, we show $g^{(2)}(t)$ observed for a single CsPbBr₃ NC.¹³⁹ The pulse repetition frequency of the excitation laser is $1/t_{\text{rep}}$ ($t_{\text{rep}} = 200$ ns). The peaks at $t \neq 0$ correspond to the case where each of two excitation pulses with time interval of t induces one photon emission. On the other hand, the center peak at $t = 0$ shows that two-photon emission is caused by one excitation pulse, which corresponds to biexciton–exciton cascade emission. In Fig. 5c, the area ratio of the center peak to the side peak at $t = \pm 200$ ns takes a small value of 0.1. This shows that one excitation pulse almost certainly leads to the single photon emission from the single CsPbBr₃ NC. A similar behavior has also been observed for MAPbBr₃ and FAPbBr₃ NCs. Therefore, independent of the A-site cation, LHP NCs possess characteristics of single photon sources.¹⁴⁵

By investigating the first photon emission at the center peak in $g^{(2)}(t)$, we can further clarify the biexciton relaxation dynamics. This is because the first photon emission is induced by the transition from the biexciton state to the exciton state. Figure 5d shows the PL dynamics of trions and the first photons.¹³⁹ This reveals that the biexciton lifetime is equal to or shorter than the time resolution of the measurement system (~ 200 ps), and is shorter than the trion lifetime of 410 ps.

Because the center peak is related to the biexciton PL, the center-peak value at weak excitation conditions ($\langle N \rangle \ll 1$) can be used to estimate the PL quantum yield (QY) of the biexciton emission. The general method reported in ref.146 is only applicable to very weak excitation conditions. In this situation, the biexciton PL can be blurred by the exciton PL because the PL QY of the biexciton emission is relatively small due to Auger recombination.

Therefore, the alternative estimation method which can be applied to rather strong excitation conditions is required. To solve this issue, a versatile method has been developed that allows us to correctly calculate the PL QY ratio of the biexciton emission to exciton emission η_{XX}/η_X from the center-to-side-peak ratio of $g^{(2)}(t)$, g_c/g_s , even under strong excitation conditions. A simultaneous measurement of the PL decay curve in addition to $g^{(2)}(t)$ can provide the PL intensity ratio of the biexciton emission to exciton emission I_{XX}/I_X and g_c/g_s , which enables the determination of η_{XX}/η_X at various excitation intensities.^{147,148} As shown in Fig. 5e, in the weak-excitation regime $\langle N \rangle \ll 1$, the two-photon cascade emission QY, η_{XX}/η_X , becomes equal to g_c/g_s and can be determined only by using $g^{(2)}(t)$. Therefore, single-dot spectroscopy can clearly distinguish the exciton and biexciton PL properties and is exceptionally useful in understanding biexciton dynamics.

The biexciton lifetime can be described by using the lifetimes of negative (τ_{X^-}) and positive (τ_{X^+}) trions as follows: $\tau_{XX}^{-1} = 2(\tau_{X^-}^{-1} + \tau_{X^+}^{-1})$ (Fig. 6a).^{140,149} A negative (positive) trion consists of an exciton with one additional electron (hole). By using this relation, the biexciton lifetime can be estimated by single-dot spectroscopy. Figure 6b shows the relation between τ_{X^-} and τ_{X^+} obtained by single-dot spectroscopy of FAPbBr₃ NCs, which is estimated to be $\tau_{X^-}/\tau_{X^+} = 1.7$.¹⁴⁰ Both of negative and positive trion states were prepared by adding a hole quencher to FAPbBr₃ NCs. Figure 6c is the histogram of the biexciton lifetimes estimated from the trion lifetimes for individual single NCs, where the average biexciton lifetime is 103 ps. This value agrees with the biexciton lifetime of 85 ps determined from transient absorption measurements of a FAPbBr₃ NC ensemble dispersed in a hexane solution. As described above, femtosecond transient absorption spectroscopy realizes a superior time resolution while single-dot spectroscopy can reduce the effects of inhomogeneity of NCs. Therefore, utilizing both of these spectroscopic methods enables us to reveal the dynamics of excitons, trions, and biexcitons in LHP NCs.

One of the phenomena where the three states of exciton, trion, and biexciton are involved, is blinking.^{61,89} As is known from conventional inorganic semiconductor NCs, *e.g.* CdSe NCs, there are two types of blinking and it can be classified into type A and type B.¹⁵⁰ In LHP NCs, these two types can also be observed.^{94,141,151} Type A is the type of PL intermittency that is characterized by two discrete states consisting of an on state with a high PL intensity (Fig. 7a; intensity region colored in red) and an intermediate state with a low PL intensity (Fig. 7a; intensity region colored in blue). On the other hand, with respect to type B, the PL intensity changes continuously and the surface charge trapping occurs (Fig. 7b).¹⁴¹

To obtain deeper understanding of these two types of blinking, Figs. 7c and d show the correlation between the PL lifetime and intensity.¹⁴¹ For type A, the PL from two states is observed: that from the exciton (X) with a high PL intensity and a long PL lifetime, and that from the trion (X⁺) with a low PL intensity and a short PL lifetime (Fig. 7c). This is also confirmed from the correlation between the PL intensity and peak energy (Fig. 7e). On the other hand, for type B, the PL intensity, lifetime, and peak energy strongly fluctuate (Figs. 7d and f). While for type A the fast component shows a clear size dependence and is caused by the biexciton or the trion, for type B no size dependence is observed for the fast component. This indicates that type B has an extrinsic origin such as surface states or the surrounding environment. This interpretation is further confirmed by the fact that by chemical modification of the NC surface, type B almost disappears and the PL quantum efficiency strongly improves.¹⁴¹

Since the first report of the two types of blinking in LHP NCs,⁹⁴ there has been a comprehensive and active discussion on the mechanisms including Auger ionization and surface traps. Figure 7g illustrates the overview of

the mechanisms: the trion formation caused by biexcitons and that caused by surface traps. In addition, a fluctuation of PL that is similar to blinking in NCs has been recently reported in the LHP micrometer-sized crystals.¹⁵²⁻¹⁵⁴ This unexpected result also suggests that further studies are required to reveal the complete picture of the underlying physics. In particular, the ionization of NCs is a very important issue in the development of light sources such as LEDs and lasers. The dynamics of ionization and neutralization have been intensively investigated, and some details are provided in refs. 142, 143, and 155. Similar approaches for CdSe-CdS core-shell NCs, *e.g.*, a core-thick-shell NC and a CdSe-CdSeS-CdS core-alloyed interface-shell NC,^{89,149,156-158} would be very useful for suppression of the Auger recombination and ionization of LHP NCs.

3.3 Biexciton binding energy

The energy level of the biexciton states is shifted due to exciton-exciton interactions, and the biexciton energy is different from the sum of two exciton energies, as illustrated in Fig. 8(a). There have been many discussions concerning the value of the biexciton binding energy ΔE_{XX} in LHP NCs. Here, note that we define ΔE_{XX} as the difference between the energy of two excitons, $2E_X$ and the biexciton energy E_{XX} , that is, $\Delta E_{XX} = 2E_X - E_{XX}$ (Fig. 8a). The exciton-exciton interaction energy Δ_{XX} is determined from the biexciton binding energy through the relation of $\Delta_{XX} = -\Delta E_{XX}$. A negative Δ_{XX} (positive ΔE_{XX}) means that the exciton-exciton interaction is attractive and the biexciton state is stable.^{62,65} On the other hand, a positive Δ_{XX} (negative ΔE_{XX}) means that the exciton-exciton interaction is repulsive.

In CsPbBr₃ NCs, it was reported that ΔE_{XX} has a huge value of about three times that of CdSe NCs and its value reaches approximately 100 meV.⁶⁹ However, in the following reports, the values of ΔE_{XX} were scattered over a wide range and the value including the sign is still under debate. It has been pointed out that the initially reported very large ΔE_{XX} of 100 meV was related to sample sintering.¹⁵⁹ In many studies, it has been reported that the exciton-exciton interaction is attractive and ΔE_{XX} is a few tens of millielectronvolt or less.^{70,74,160-162}

The value of ΔE_{XX} has been mainly investigated by using transient absorption spectroscopy and time-resolved PL spectroscopy of NC ensembles. The reported values in CsPbBr₃ NCs are scattered over a wide range^{69,160,161} and even a negative value (the repulsive exciton-exciton interaction) has been reported.¹⁶³ One of the reasons for such inconsistencies should be that the measurements were performed on NC ensembles, which have a finite NC size distribution. Because ΔE_{XX} depends on the NC size and the excitation energy,^{69,70,74,164,165} a significant influence of the size distribution of the measured NCs is considered to appear. By using polarization-dependent two-dimensional spectroscopy, it has recently reported that the size-dependent biexciton binding energy in CsPbBr₃ NCs can be determined even with NC ensembles and ΔE_{XX} is estimated to be less than about 40 meV with ΔE_{XX} being positive, *i.e.* the attractive exciton-exciton interaction (Fig. 8b).⁷³

With the ability to obtain the PL spectrum of a single NC, single-dot spectroscopy is a powerful method that can directly measure the NC-size dependence of ΔE_{XX} .^{122,134} The PL linewidth of ensemble NCs at room temperature is relatively broad because of the interaction with phonons and the NC-size distribution. In contrast, the PL spectra of single NCs at low temperature show narrow PL linewidths, which enables a high precision measurement of ΔE_{XX} . Figure 8c shows the PL spectrum of a single FAPbBr₃ NC at 5.5 K.¹³⁴ On the low-energy side of the exciton emission peak, four emission peaks are observed, which are characterized by the trion and

biexciton PL and two LO phonon replicas. The biexciton emission energy corresponds to the biexciton–exciton transition energy as shown in the inset of Fig. 8c. Because the biexciton–exciton transition energy is shifted from the exciton energy by ΔE_{XX} , ΔE_{XX} can be estimated from the difference between the peak energies of the biexciton and exciton emission spectra. The binding energy of the trion can be determined in the same way. Figure 8d shows the observed NC-size dependence of the binding energies of trions and biexcitons. As the NC size becomes smaller, both of the trion and biexciton energies increase. Such a size-dependent biexciton binding energy has also been observed in CsPbBr₃ NCs.^{69,73} Moreover, the size dependence of the biexciton binding energy has been also observed for CuCl¹³¹ and CdSe/ZnS NCs¹⁶⁴ and theoretically calculated¹⁶⁵. Figure 8e plots the normalized biexciton binding energy of several inorganic semiconductor NCs as a function of the normalized NC size, where the binding energy and the size are normalized by the bulk exciton binding energy and the exciton Bohr radius, respectively. It can be seen that the normalized biexciton binding energy in LHP NCs is on the same level as those in other representative inorganic semiconductor NCs, and that the normalized size dependence shows the same behavior irrespective of the semiconductor materials. We note that in single-dot spectroscopy measurements at low temperatures, all biexciton binding energies are observed to be positive and thus the exciton–exciton interaction is attractive.

4. Hot–biexciton effect and control of optical gain

4.1. Exciton–exciton interactions and optical gain dynamics

CsPbX₃ NCs show excellent properties for optical gain media such as high PL quantum efficiencies exceeding 90% and low-threshold light amplification in the entire visible region.^{53,57,58} Biexcitons play a significant role in nonlinear optical responses such as light amplification and thus the optical gain is strongly influenced by exciton–exciton interactions.⁶²⁻⁷⁴ Because the biexciton dynamics in LHP NCs are very fast, femtosecond transient absorption spectroscopy is suitable to investigate the optical gain dynamics.

In Fig. 9a, we show the change in the absorption spectrum $-\Delta ad$ of CsPbI₃ NCs (an average edge length of 7.0 nm) at different pump-probe delay times t_{pp} , where the pump intensity is set to be $\langle N \rangle = 0.1$ and the pump photon energy corresponds to the excess energy E_{ex} of 0.47 eV.⁷⁰ E_{ex} is the difference between the pump photon energy and the band-edge exciton energy. A long-lasting ($t_{pp} > 500$ ps) bleaching signal ($-\Delta ad > 0$) appears around the band-edge due to the state-filling effect as described in Fig. 4a. In addition to this bleaching signal, an induced absorption signal ($-\Delta ad < 0$) appears immediately after excitation ($t_{pp} < 2$ ps) on the low-energy side of the band-edge. The induced absorption signal is ascribed to the biexciton effect.^{62,70,74,138,160} The biexciton effect can be described as follows (Fig. 9b). First, a hot exciton with an excess energy of E_{ex} is generated by the pump pulse. This hot exciton and the band-edge exciton generated by the probe pulse interact with each other via a Coulomb interaction. Consequently, the band-edge transition energy shifts from E_g to $E_g + \Delta_{XX}$, where E_g is the band-edge transition energy under the absence of the hot exciton. Because the exciton–exciton interaction in CsPbI₃ NCs is attractive ($\Delta_{XX} < 0$), the band-edge transition redshifts. While the relaxation of the hot exciton is not completed (0 ps $< t_{pp} < 2$ ps), this redshift brings about the induced absorption and bleaching signals around the band edge, which results in a derivative-like feature of $-\Delta ad$. On the other hand, after the relaxation of the hot exciton ($t_{pp} > 2$ ps), a strong bleaching signal appears near the band edge due to the state-filling effect, and the induced absorption signal

disappears.

Figure 9c plots the E_{ex} dependence of Δ_{XX} . It can be seen that Δ_{XX} takes negative values, and $|\Delta_{\text{XX}}|$ increases monotonically and reaches a constant value as E_{ex} is increased. This clearly shows that the strength of the exciton–exciton interaction between the hot exciton and the band-edge exciton depends on the hot-exciton state.⁷⁰ The hot-exciton-state-dependent exciton–exciton interaction significantly influences the optical gain behavior. In Fig. 9d, we show the nonlinear absorption spectra $\alpha_{\text{NL}}d = \alpha_0d + \Delta\alpha d$ (α_0d : steady-state absorption spectrum) immediately after excitation ($t_{\text{pp}} = 0.3$ ps) for $\langle N \rangle = 1$ and different values of E_{ex} . For $E_{\text{ex}} = 0.05$ eV, $\alpha_{\text{NL}}d$ is smaller than zero at probe photon energies below 1.80 eV, showing that optical gain occurs. On the other hand, with increasing E_{ex} , the optical gain spectral region redshifts and vanishes. Moreover, in Fig. 9e, we show the t_{pp} dependence of the normalized change in the absorption spectrum $-\Delta\alpha/\alpha_0$ at the probe photon energy of 1.80 eV. It can be seen that t_{pp} when the optical gain appears ($-\Delta\alpha/\alpha_0 > 1$) is longer for larger E_{ex} . This results from the fact that the induced absorption signal immediately after excitation suppresses the optical gain. These findings show that the optical gain is significantly modulated by the hot-exciton state through the exciton–exciton interactions, which suggests a novel approach to the optical gain control on the picosecond time scale.

4.2. Optical gain control by symmetry engineering of multiexciton states

As we mentioned above, the optical gain in LHP NCs can be controlled by exciton–exciton interactions which depend on the excited state. Therefore, an improvement of the optical gain is expected by manipulating the excited state. Because double-pump transient absorption spectroscopy can realize various excited states, the symmetry of hot excitons and hot biexcitons can be controlled and the optical gain dynamics can be further clarified.⁷⁴ In Fig. 10a, we provide a brief description of this method. Excitons are generated by the first and second pump pulses, which have the same intensity and are separated by a time interval Δt . The dynamics of the optical gain spectra are measured by a white-light probe pulse separated from the second pump pulse by a time interval t . In the case of a single pump excitation, either a hot exciton or a symmetric hot biexciton (which consists of a pair of hot excitons with equal energy) is formed immediately after excitation (Fig. 10b). On the other hand, in the case of a double-pump excitation, after the hot exciton generated by the first pump relaxes to a ground exciton state, it is possible to generate an asymmetric hot biexciton via the additional excitation by the second pump (Fig. 10b). An asymmetric hot biexciton is a state in which one hot exciton and one band-edge exciton exist within a single NC. In Fig. 10b, $\Delta^{(i)}_{\text{XX}}$ denotes the band-edge exciton energy shift under the presence of i ($i = \text{h, hh, g, and hg}$) state, where h, hh, g, and hg mean a hot exciton, a symmetric hot biexciton, a band-edge exciton, and an asymmetric hot biexciton, respectively.

Figure 10c shows the Δt dependence of Δ_{XX} in CsPbI₃ NCs, where Δ_{XX} contains contributions from all excited states. The intensities of the first and second pump pulses, $\langle N_{1\text{st}} \rangle$ and $\langle N_{2\text{nd}} \rangle$, are fixed to $\langle N_{1\text{st}} \rangle = \langle N_{2\text{nd}} \rangle = 2$. By fitting to the Δt dependence of Δ_{XX} with a model considering contributions from all excited states, we obtained the values $\Delta^{(\text{h+hh})}_{\text{XX}} = -36 \pm 2$ meV, $\Delta^{(\text{g})}_{\text{XX}} = -3 \pm 6$ meV, and $\Delta^{(\text{hg})}_{\text{XX}} = -27 \pm 4$ meV. For asymmetric hot biexcitons, the absolute value of the energy shift becomes smaller than the values for hot excitons and symmetric hot biexcitons. The larger the redshift of the band-edge exciton energy due to the interaction between excitons becomes, the larger is the reabsorption of amplified light, which leads to lowering of the optical gain performance.

If a double-pump pulse can generate an excited state which provides a small band-edge energy shift, the optical gain performance would be improved. Therefore, we estimated the optical gain threshold $\langle N_g \rangle$ in CsPbI₃ NCs for the cases of single- and double-pump measurements. Figure 10d plots the Δt dependence of the estimated $\langle N_g \rangle$. It can be seen that $\langle N_g \rangle$ at around $\Delta t = 0$ ps agrees with $\langle N_g \rangle$ for single-pump measurements ($\langle N_g \rangle = 7.3$). As Δt is increased, $\langle N_g \rangle$ becomes smaller than the value for single-pump measurements at $\Delta t = 10 \sim 30$ ps and then starts to increase monotonically.

Such a Δt dependence of $\langle N_g \rangle$ can be understood by considering the excited state dynamics. In the single-pump experiment, the presence of hot excitons and symmetric hot biexcitons suppresses the optical gain immediately after the excitation. On the other hand, in the double-pump experiment, the fraction of asymmetric hot biexcitons is more significant. Because asymmetric hot biexcitons show a small energy shift, the effective band-edge energy shift becomes smaller. Therefore, the reabsorption effect becomes weaker and the optical gain threshold is lowered ($\Delta t < 30$ ps). When Δt is increased further, the time interval between the first pump pulse and the probe pulse starts to become longer than the biexciton lifetime ($\tau_{XX} = 60$ ps). This leads to an increase in the fraction of the biexcitons that recombine before the probe pulse arrives. Therefore, as Δt is increased, the fraction of the biexcitons contributing to the optical gain decreases, and thus the effective optical gain threshold increases ($\Delta t > 100$ ps). Consequently, in double-pump transient absorption spectroscopy, the competition between the two effects changes depending on the pump interval Δt , which decreases or increases the optical gain threshold, and a reduction of the optical gain threshold is realized in a specific time range.

In the above, we mentioned that the relaxation of hot excitons or hot carriers is important for biexciton properties and also for the optical gain. In addition, it has been reported that, compared to the conventional inorganic semiconductors, the intra-band relaxation of photoexcited carriers in LHPs is very slow, that is, the hot carriers possess a long lifetime.¹⁶⁶⁻¹⁷³ The electron–lattice interactions in LHPs are very unique, and a peculiar hot-phonon bottleneck effect has been observed. Because the hot-phonon bottleneck effect significantly influences the exciton and photocarrier behaviors,^{174,175} these observations revealed that LHPs are materials where hot-carrier and hot-exciton effects can be clearly observed, and they are promising materials systems for hot-carrier-based optoelectronic applications. Hot carrier relaxation in LHPs was reported to be characterized by a slow relaxation time constant of a few tens of picoseconds under strong excitation conditions, which is about three orders of magnitude longer than in bulk GaAs under the same excitation conditions.^{11,167} This shows that when the carriers have a large excess energy at high excitation densities, the relaxation time constant becomes slow. The increase of the hot-carrier lifetime in high-density carrier systems is very similar to the results previously observed in III–V quantum wells and can be understood in terms of a hot-phonon bottleneck mechanism. If the decay of LO phonons into acoustic phonons is suppressed, the LO phonons are again absorbed by carriers and a high carrier temperature is maintained. Several possible origins of the hot-phonon bottleneck effect in LHPs have been proposed, and an overview is provided in refs. 10 and 11. Although there are many unresolved issues on the hot-carrier relaxation dynamics in LHPs, it is most likely true that the characteristic phonon modes of LHPs with the strong electron–lattice interactions and strong anharmonicity play important roles. By utilizing the long-lived hot carriers, LHP-based novel optical devices are expected in the future.

5. Conclusions and perspectives

We have reviewed the recent results on the biexciton dynamics in LHP NCs, which are attracting considerable interest as next-generation photonic and optoelectronic materials. Related to the electronic structure of LHP semiconductors, the optical responses of these NCs are governed by the dynamics of excitons, trions, and biexcitons. This has been revealed by femtosecond transient absorption spectroscopy, time-resolved PL spectroscopy, and single-dot spectroscopy. The biexciton has a short lifetime of a few tens of picoseconds due to Auger recombination, which results in the suppression of the two-photon emission via the biexciton–exciton radiative cascade. Single-dot spectroscopy has shown that LHP NCs have superior characteristics for single-photon sources. Moreover, we discussed that it is possible to control and improve the optical gain characteristics by manipulating the excited biexciton state, which is revealed by using single- and double-pump transient absorption spectroscopy. In terms of device applications, non-radiative Auger recombination process of biexcitons mostly leads to efficiency reduction of devices such as LEDs and lasers. On the other hand, the optical gain controllability through exciton–exciton interactions in LHP NCs would realize novel photonics devices, such as ultra-fast optical switches and low-threshold lasers.

The biexciton-symmetry dependence of exciton–exciton interactions provides a new way to control and improve the optical gain. At the same time, this property would also be beneficial for quantum information applications, such as sources of indistinguishable single photons and entangled photon pairs. Recently, a peculiar exciton fine structure originating from the Rashba effect has been reported for CsPbX₃ NCs.¹⁰⁰ Due to this characteristic structure, short radiative lifetimes and long optical coherence times have been observed and these properties show the great potential of CsPbX₃ NCs for next-generation quantum emitters.¹⁷⁶ However, if a non-degenerate exciton level is formed by exciton fine-structure splitting, a two-photon entanglement via a biexciton–exciton cascade emission is inhibited.^{177,178} Therefore, in order to obtain entangled photon pairs, the exciton fine structure should be controlled by applying external fields such as magnetic field¹⁷⁹, light¹⁷⁸, etc. On the other hand, it has been proposed that, even if a non-degenerate exciton level exists, entangled photon pairs can be obtained if the biexciton–exciton transition energy is equal to the exciton energy.^{180,181} Such an exciton- and biexciton-energy control has been realized by applying biaxial strain.¹⁸² Control of the biexciton binding energy via the biexciton symmetry engineering would become an alternative approach to the conventional energy-state control method.

With their long hot-carrier lifetimes, LHPs are promising materials for fabrication of novel hot-carrier devices. For such applications, a detailed understanding of the biexciton symmetry and the exciton–exciton interactions is crucial. Therefore, we hope that a theoretical framework will be established that describes the biexciton-symmetry-dependent exciton–exciton interactions by considering the extension and overlap of the electron and hole wavefunctions in a NC together with the electronic structure of LHPs.

In addition to a simple cubic shape, various nanostructure shapes of LHPs have also been fabricated, including nanoplatelets^{55,183,184} and atomically thin 2D perovskites¹⁸⁵⁻¹⁸⁷. Therefore, it is expected that the electronic structure and the exciton dynamics in such LHP nanostructures will be clarified and that new optical functionalities will be developed. In fact, in addition to characteristic exciton properties¹⁸⁸, unique spin-related optical responses, such as chiral-induced spin selectivity¹⁸⁹ and formation of spin-polarized exciton halo¹⁹⁰, have recently been observed. One

of new research directions is the exciton physics at homo- and hetero-interfaces of atomically thin LHP films. These materials systems are expected to become important as novel two-dimensional materials beyond transition metal dichalcogenides. In addition, a growing number of ferroelectric 2D perovskites has been reported.¹⁹¹ Thus, another research direction is the study of photophysics coupled to ferroelectricity. Such ferroelectricity-related optical responses have recently been investigated in a metal-free ferroelectric halide perovskite,¹⁹² which exhibits both visible PL and ferroelectricity, and visible PL correlated with local ferroelectricity has been observed.¹⁹³ The detail characterization of the fundamental physical properties by precise laser spectroscopy will become even more important in the future.

References

1. S. D. Stranks and H. J. Snaith, Metal-halide perovskites for photovoltaic and light-emitting devices, *Nat. Nanotechnol.*, 2015, **10**, 391–402.
2. J. Even, L. Pedesseau, C. Katan, M. Kepenekian, J.-S. Lauret, D. Saponi and E. Deleporte, Solid-state physics perspective on hybrid perovskite semiconductors, *J. Phys. Chem. C*, 2015, **119**, 10161–10177.
3. B. R. Sutherland and E. H. Sargent, Perovskite photonic sources, *Nat. Photonics*, 2016, **10**, 295–302.
4. L. M. Herz, Charge-Carrier Dynamics in Organic-Inorganic Metal Halide Perovskites, *Annu. Rev. Phys. Chem.*, 2016, **67**, 65–89.
5. K. Miyata, T. L. Atallah and X.-Y. Zhu, Lead halide perovskites: crystal-liquid duality, phonon glass electron crystals, and large polaron formation, *Sci. Adv.*, 2017, **3**, e1701469.
6. Y. Yamada, T. Yamada and Y. Kanemitsu, Free carrier radiative recombination and photon recycling in lead halide perovskite solar cell materials, *Bull. Chem. Soc. Jpn.*, 2017, **90**, 1129–1140.
7. Y. Kanemitsu and T. Handa, Photophysics of metal halide perovskites: from materials to devices, *Jpn. J. Appl. Phys.*, 2018, **57**, 090101.
8. C. Katan, A. D. Mohite and J. Even, Entropy in halide perovskites, *Nat. Mater.*, 2018, **17**, 377–379.
9. Y. Jiang, X. Wang and A. Pan, Properties of excitons and photogenerated charge carriers in metal halide perovskites, *Adv. Mater.*, 2019, **31**, 1806671.
10. M. Li, J. Fu, Q. Xu and T. C. Sum, Slow Hot-Carrier Cooling in Halide Perovskites: Prospects for Hot-Carrier Solar Cells, *Adv. Mater.*, 2019, **31**, 1802486.
11. P. P. Joshi, S. F. Maehrlein and X.-Y. Zhu, Dynamic Screening and Slow Cooling of Hot Carriers in Lead Halide Perovskites. *Adv. Mater.* 2019, **31**, 1803054.
12. Y. Kanemitsu, T. Yamada, T. Handa and M. Nagai, Optical responses of lead halide perovskite semiconductors, *Semicond. Sci. Technol.*, 2020, **35**, 093001.
13. M. Baranowski and P. Plochocka, Excitons in metal halide perovskites, *Adv. Energy Mater.*, 2020, **10**, 1903659.
14. T. Handa, T. Yamada, M. Nagai and Y. Kanemitsu, Phonon, thermal, and thermo-optical properties of halide perovskites, *Phys. Chem. Chem. Phys.*, 2020, **22**, 26069.
15. R. Su, A. Fieramosca, Q. Zhang, H. S. Nguyen, E. Deleporte, Z. Chen, D. Sanvitto, T. C. H. Liew and Q. Xiong, Perovskite semiconductors for room-temperature exciton polaritonics, *Nat. Mater.*, 2021, **20**, 1315–

1324.

16. Y. Yamada and Y. Kanemitsu. Electron–phonon interactions in halide perovskites. *NPG Asia Mater.*, 2022, **14**, 48.
17. A. Kojima, K. Teshima, Y. Shirai and T. Miyasaka, Organometal Halide Perovskites as Visible-Light Sensitizers for Photovoltaic Cells, *J. Am. Chem. Soc.*, 2009, **131**, 6050–6051.
18. M. M. Lee, J. Teuscher, T. Miyasaka, T. N. Murakami and H. J. Snaith, Efficient hybrid solar cells based on meso-superstructured organometal halide perovskites, *Science*, 2012, **338**, 643–647.
19. H.-S. Kim, C.-R. Lee, J.-H. Im, K.-B. Lee, T. Moehl, A. Marchioro, S.-J. Moon, R. Humphry-Baker, J.-H. Yum, J. E. Moser, M. Grätzel and N.-G. Park, Lead iodide perovskite sensitized all-solid-state submicron thin film mesoscopic solar cell with efficiency exceeding 9%, *Sci. Rep.*, 2012, **2**, 591.
20. N. J. Jeon, J. H. Noh, Y. C. Kim, W. S. Yang, S. Ryu and S. I. Seok, Solvent engineering for high-performance inorganic-organic hybrid perovskite solar cells, *Nat. Mater.*, 2014, **13**, 897–903.
21. Y. Kanemitsu, Luminescence spectroscopy of lead-halide perovskites: materials properties and application as photovoltaic devices, *J. Mater. Chem. C*, 2017, **5**, 3427–3437.
22. T. Handa, A. Wakamiya and Y. Kanemitsu, Photophysics of lead-free tin halide perovskite films and solar cells, *APL Mater.*, 2019, **7**, 080903.
23. J. P. Correa-Baena, M. Saliba, T. Buonassisi, M. Grätzel, A. Abate, W. Tress and A. Hagfeldt, Promises and challenges of perovskite solar cells, *Science*, 2018, **358**, 739–44.
24. Y. Rong, Y. Hu, A. Mei, H. Tan, M. I. Saidaminov, S. I. Seok, M. D. McGehee, E. H. Sargent and H. Han, Challenges for commercializing perovskite solar cells. *Science*, 2018, **361**, eaat8235.
25. J. W. Lee, S. Tan, S. I. Seok, Y. Yang and N. G. Park, Rethinking the A cation in halide perovskites. *Science*, 2022, **375**, eabj1186.
26. M. A. Green, E. D. Dunlop, J. Hohl-Ebinger, M. Yoshita, N. Kopidakis and X. Hao, Solar cell efficiency tables (version 59), *Prog. Photovoltaics*, 2022, **30**, 3.
27. S. D. Stranks, G. E. Eperon, G. Grancini, C. Menelaou, M. J. P. Alcocer, T. Leijtens, L. M. Herz, A. Petrozza and H. J. Snaith, Electron-hole diffusion lengths exceeding 1 micrometer in an organometal trihalide perovskite absorber, *Science*, 2013, **342**, 341–344.
28. G. Xing, N. Mathews, S. Sun, S. S. Lim, Y. M. Lam, M. Grätzel, S. Mhaisalkar and T. C. Sum, Long-range balanced electron- and hole-transport lengths in organic-inorganic $\text{CH}_3\text{NH}_3\text{PbI}_3$, *Science*, 2013, **342**, 344–347.
29. Y. Yamada, T. Nakamura, M. Endo, A. Wakamiya and Y. Kanemitsu, Near-band-edge optical responses of solution-processed organic–inorganic hybrid perovskite $\text{CH}_3\text{NH}_3\text{PbI}_3$ on mesoporous TiO_2 electrodes, *Appl. Phys. Express*, 2014, **7**, 032302.
30. A. M. A. Leguy, P. Azarhoosh, M. I. Alonso, M. Campoy-Quiles, O. J. Weber, J. Yao, D. Bryant, M. T. Weller, J. Nelson, A. Walsh, M. van Schilfgaarde and P. R. F. Barnes, Experimental and theoretical optical properties of methylammonium lead halide perovskites, *Nanoscale*, 2016, **8**, 6317–6327.
31. M. Shirayama, H. Kadowaki, T. Miyadera, T. Sugita, M. Tamakoshi, M. Kato, T. Fujiseki, D. Murata, S. Hara, T. N. Murakami, S. Fujimoto, M. Chikamatsu and H. Fujiwara, Optical Transitions in Hybrid Perovskite Solar Cells: Ellipsometry, Density Functional Theory, and Quantum Efficiency Analyses for

- CH₃NH₃PbI₃, *Phys. Rev. Appl.*, 2016, **5**, 014012.
32. Y. Yamada, T. Nakamura, M. Endo, A. Wakamiya and Y. Kanemitsu, Photocarrier recombination dynamics in perovskite CH₃NH₃PbI₃ for solar cell applications, *J. Am. Chem. Soc.*, 2014, **136**, 11610-11613.
 33. S. D. Stranks, V. M. Burlakov, T. Leijtens, J. M. Ball, A. Goriely and H. J. Snaith, Recombination kinetics in organic-inorganic perovskites: Excitons, free charge, and subgap states, *Phys. Rev. Appl.*, 2014, **2**, 034007.
 34. Y. Yamada, T. Yamada, L. Q. Phuong, N. Maruyama, H. Nishimura, A. Wakamiya, Y. Murata and Y. Kanemitsu, Dynamic optical properties of CH₃NH₃PbI₃ single crystals as revealed by one- and two-photon excited photoluminescence measurements, *J. Am. Chem. Soc.*, 2015, **137**, 10456-10459.
 35. T. Yamada, Y. Yamada, Y. Nakaike, A. Wakamiya and Y. Kanemitsu, Photon emission and reabsorption processes in CH₃NH₃PbBr₃ single crystals revealed by time-resolved two-photon-excitation photoluminescence microscopy, *Phys. Rev. Appl.*, 2017, **7**, 014001.
 36. T. Yamada, Y. Yamada and Y. Kanemitsu, Photon recycling in perovskite CH₃NH₃PbX₃ (X = I, Br, Cl) bulk single crystals and polycrystalline films, *J. Lumin.* 2020, **220**, 116987.
 37. L.M. Pazos-Outon, M. Szumilo, R. Lamboll, J.M. Richter, M. Crespo-Quesada, M. Abdi Jalebi, H.J. Beeson, M. Vruini, M. Alsari, H.J. Snaith, B. Ehrler, R.H. Friend and F. Deschler, Photon recycling in lead iodide perovskite solar cells, *Science*, 2016, **351**, 1430.
 38. F. Deschler, M. Price, S. Pathak, L. E. Klintberg, D.-D. Jarausch, R. Higler, S. Hüttner, T. Leijtens, S. D. Stranks, H. J. Snaith, M. Atatüre, R. T. Phillips and R. H. Friend, High photoluminescence efficiency and optically pumped lasing in solution-processed mixed halide perovskite semiconductors, *J. Phys. Chem. Lett.*, 2014, **5**, 1421-1426.
 39. T. Yamada, T. Handa, Y. Yamada and Y. Kanemitsu, Light emission from halide perovskite semiconductors: Bulk crystals, thin films, and nanocrystals, *J. Phys. D: Appl. Phys.*, 2021, **54**, 383001.
 40. B. Wenger, P. K. Nayak, X. Wen, S. V. Kesava, N. K. Noel and H. J. Snaith, Consolidation of the optoelectronic properties of CH₃NH₃PbBr₃ perovskite single crystals. *Nat. Commun.*, 2017, **8**, 590.
 41. T. Handa, H. Tahara, T. Aharen and Y. Kanemitsu, Large negative thermo-optic coefficients of a lead halide perovskite, *Sci. Adv.*, 2019, **5**, eaax0786.
 42. L. Dou, Y. Yang, J. You, Z. Hong, W.-H. Chang, G. Li and Y. Yang, Solution-processed hybrid perovskite photodetectors with high detectivity, *Nat. Commun.*, 2014, **5**, 5404.
 43. S. Yakunin, M. Sytnyk, D. Kriegner, S. Shrestha, M. Richter, G. J. Matt, H. Azimi, C. J. Brabec, J. Stangl, M. V. Kovalenko and W. Heiss, Detection of X-ray photons by solution-processed lead halide perovskites, *Nat. Photonics*, 2015, **9**, 444-449.
 44. Z.-K. Tan, R. S. Moghaddam, M. L. Lai, P. Docampo, R. Higler, F. Deschler, M. Price, A. Sadhanala, L. M. Pazos, D. Credgington, F. Hanusch, T. Bein, H. J. Snaith and R. H. Friend, Bright light-emitting diodes based on organometal halide perovskite, *Nat. Nanotechnol.*, 2014, **9**, 687-692.
 45. G. Xing, N. Mathews, S. S. Lim, N. Yantara, X. Liu, D. Sabba, M. Graetzel, S. Mhaisalkar and T. C. Sum, Low-temperature solution-processed wavelength-tunable perovskites for lasing, *Nat. Mater.*, 2014, **13**, 476-480.
 46. H. Tahara, T. Aharen, A. Wakamiya and Y. Kanemitsu, Photorefractive Effect in Organic-Inorganic Hybrid

- Perovskites and Its Application to Optical Phase Shifter, *Adv. Opt. Mater.*, 2018, **6**, 1701366.
47. H. Hirori, P. Xia, Y. Shinohara, T. Otobe, Y. Sanari, H. Tahara, N. Ishii, J. Itatani, K. L. Ishikawa, T. Aharen, M. Ozaki, A. Wakamiya and Y. Kanemitsu, High-order harmonic generation from hybrid organic–inorganic perovskite thin films, *APL Mater.*, 2019, **7**, 041107.
 48. M. V. Kovalenko, L. Protesescu, and M. I. Bodnarchuk, Properties and potential optoelectronic applications of lead halide perovskite nanocrystals, *Science*, 2017, **358**, 745-750.
 49. Q. A. Akkerman, G. Rainò, M. V. Kovalenko and L. Manna, Genesis, challenges and opportunities for colloidal lead halide perovskite nanocrystals, *Nat. Mater.*, 2018, **17**, 394-405.
 50. J. Shamsi, A. S. Urban, M. Imran, L. De Trizio and L. Manna, Metal Halide Perovskite Nanocrystals: Synthesis, Post-Synthesis Modifications, and Their Optical Properties, *Chem. Rev.*, 2019, **119**, 3296-3348.
 51. F. P. García de Arquer, D. V. Talapin, V. Klimov, Y. Arakawa, M. Bayer and E. H. Sargent, Semiconductor quantum dots: Technological progress and future challenges, *Science*, 2021, **373**, eaaz8541.
 52. L. C. Schmidt, A. Pertegás, S. González-Carrero, O. Malinkiewicz, S. Agouram, G. Mínguez Espallargas, H. J. Bolink, R. E. Galian and J. Pérez-Prieto, Nontemplate synthesis of $\text{CH}_3\text{NH}_3\text{PbBr}_3$ perovskite nanoparticles, *J. Am. Chem. Soc.*, 2014, **136**, 850-853.
 53. L. Protesescu, S. Yakunin, M. I. Bodnarchuk, F. Krieg, R. Caputo, C. H. Hendon, R. X. Yang, A. Walsh and M. V. Kovalenko, Nanocrystals of cesium lead halide perovskites (CsPbX_3 , X = Cl, Br, and I): Novel optoelectronic materials showing bright emission with wide color gamut, *Nano Lett.*, 2015, **15**, 3692-3696.
 54. G. Rainò, M. A. Becker, M. I. Bodnarchuk, R. F. Mahrt, M. V. Kovalenko and T. Stöferle, Superfluorescence from lead halide perovskite quantum dot superlattices, *Nature*, 2018, **563**, 671-675.
 55. J. A. Sichert, Y. Tong, N. Mutz, M. Vollmer, S. Fischer, K. Z. Milowska, R. García Cortadella, B. Nickel, C. Cardenas-Daw, J. K. Stolarczyk, A. S. Urban and J. Feldmann, Quantum Size Effect in Organometal Halide Perovskite Nanoplatelets. *Nano Lett.*, 2015, **15**, 6521.
 56. Q. A. Akkerman, V. D’Innocenzo, S. Accornero, A. Scarpellini, A. Petrozza, M. Prato and L. Manna, Tuning the optical properties of cesium lead halide perovskite nanocrystals by anion exchange reactions, *J. Am. Chem. Soc.*, 2015, **137**, 10276-10281.
 57. Y. Wang, X. Li, J. Song, L. Xiao, H. Zeng and H. Sun, All-inorganic colloidal perovskite quantum dots: A new class of lasing materials with favorable characteristics, *Adv. Mater.*, 2015, **27**, 7101-7108.
 58. S. Yakunin, L. Protesescu, F. Krieg, M. I. Bodnarchuk, G. Nedelcu, M. Humer, G. De Luca, M. Fiebig, W. Heiss and M. V. Kovalenko, Low-threshold amplified spontaneous emission and lasing from colloidal nanocrystals of caesium lead halide perovskites, *Nat. Commun.*, 2015, **6**, 8056.
 59. X. Li, Y. Wu, S. Zhang, B. Cai, Y. Gu, J. Song and H. Zeng, CsPbX_3 quantum dots for lighting and displays: Room-temperature synthesis, photoluminescence superiorities, underlying origins and white light-emitting diodes, *Adv. Funct. Mater.*, 2016, **26**, 2435-2445.
 60. M. Yuan, L. N. Quan, R. Comin, G. Walters, R. Sabatini, O. Voznyy, S. Hoogland, Y. Zhao, E. M. Beauregard, P. Kanjanaboos, Z. Lu, D. H. Kim and E. H. Sargent, Perovskite energy funnels for efficient light-emitting diodes, *Nat. Nanotechnol.*, 2016, **11**, 872-877.
 61. Y. Kanemitsu, Trion dynamics in lead halide perovskite nanocrystals, *J. Chem. Phys.*, 2019, **151**, 170902.

62. V. I. Klimov, Spectral and dynamical properties of multiexcitons in semiconductor nanocrystals, *Annu. Rev. Phys. Chem.*, 2007, **58**, 635-673.
63. V. I. Klimov, A. A. Mikhailovsky, S. Xu, A. Malko, J. A. Hollingsworth, C. A. Leatherdale, H. J. Eisler and M. G. Bawendi, Optical gain and stimulated emission in nanocrystal quantum dots, *Science*, 2000, **290**, 314-317.
64. U. Woggon, O. Wind, F. Gindele, E. Tsitsishvili and M. Müller, Optical transitions in cdse quantum dots: From discrete levels to broad gain spectra, *J. Lumin.*, 1996, **70**, 269-280.
65. V. I. Klimov, S. A. Ivanov, J. Nanda, M. Achermann, I. Bezel, J. A. McGuire and A. Piryatinski, Single-exciton optical gain in semiconductor nanocrystals, *Nature*, 2007, **447**, 441-446.
66. R. R. Cooney, S. L. Sewall, D. M. Sagar and P. Kambhampati, Gain control in semiconductor quantum dots via state-resolved optical pumping, *Phys. Rev. Lett.*, 2009, **102**, 127404.
67. S. L. Sewall, R. R. Cooney, E. A. Dias, P. Tyagi and P. Kambhampati, State-resolved observation in real time of the structural dynamics of multiexcitons in semiconductor nanocrystals, *Phys. Rev. B*, 2011, **84**, 235304.
68. H. Jung, N. Ahn and V. I. Klimov, Prospects and challenges of colloidal quantum dot laser diodes. *Nat. Photonics*, 2021, **15**, 643-655.
69. J. A. Castañeda, G. Nagamine, E. Yassitepe, L. G. Bonato, O. Voznyy, S. Hoogland, A. F. Nogueira, E. H. Sargent, C. H. B. Cruz and L. A. Padilha, Efficient biexciton interaction in perovskite quantum dots under weak and strong confinement, *ACS Nano*, 2016, **10**, 8603-8609.
70. G. Yumoto, H. Tahara, T. Kawawaki, M. Saruyama, R. Sato, T. Teranishi and Y. Kanemitsu, Hot biexciton effect on optical gain in CsPbI₃ perovskite nanocrystals, *J. Phys. Chem. Lett.*, 2018, **9**, 2222-2228.
71. G. Nagamine, J. O. Rocha, L. G. Bonato, A. F. Nogueira, Z. Zaharieva, A. A. R. Watt, C. H. de Brito Cruz and L. A. Padilha, Two-photon absorption and two-photon-induced gain in perovskite quantum dots, *J. Phys. Chem. Lett.*, 2018, **9**, 3478-3484.
72. W. Zhao, Z. Qin, C. Zhang, G. Wang, X. Huang, B. Li, X. Dai and M. Xiao, Optical gain from biexcitons in CsPbBr₃ nanocrystals revealed by two-dimensional electronic spectroscopy, *J. Phys. Chem. Lett.*, 2019, **10**, 1251-1258.
73. X. Huang, L. Chen, C. Zhang, Z. Qin, B. Yu, X. Wang and M. Xiao, Inhomogeneous biexciton binding in perovskite semiconductor nanocrystals measured with two-dimensional spectroscopy, *J. Phys. Chem. Lett.*, 2020, **11**, 10173-10181.
74. E. Kobiyama, H. Tahara, R. Sato, M. Saruyama, T. Teranishi and Y. Kanemitsu, Reduction of optical gain threshold in CsPbI₃ nanocrystals achieved by generation of asymmetric hot-biexcitons, *Nano Lett.*, 2020, **20**, 3905-3910.
75. R. D. Schaller and V. I. Klimov, High efficiency carrier multiplication in PbSe nanocrystals: implications for solar energy conversion, *Phys. Rev. Lett.*, 2004, **92**, 186601.
76. R. J. Ellingson, M. C. Beard, J. C. Johnson, P. Yu, O. I. Micic, A. J. Nozik, A. Shabaev and Al. L. Efros, Highly efficient multiple exciton generation in colloidal PbSe and PbS quantum dots. *Nano Lett.*, 2005, **5**, 865-871.
77. A. Ueda, K. Matsuda, T. Tayagaki and Y. Kanemitsu, Carrier multiplication in carbon nanotubes studied by

- femtosecond pump-probe spectroscopy, *Appl. Phys. Lett.*, 2008, **92**, 233105.
78. S. Wang, M. Khafizov, X. Tu, M. Zheng and T. D. Krauss, Multiple exciton generation in single-walled carbon nanotubes, *Nano Lett.*, 2010, **10**, 2381-2386.
 79. Y. Kanemitsu, Multiple exciton generation and recombination in carbon nanotubes and nanocrystals, *Acc. Chem. Res.*, 2013, **46**, 1358-1366.
 80. A. Shabaev, C. S. Hellberg and Al. L. Efros, Efficiency of multiexciton generation in colloidal nanostructures. *Acc. Chem. Res.*, 2013, **46**, 1242-1251.
 81. H. Tahara, M. Sakamoto, T. Teranishi and Y. Kanemitsu, Harmonic quantum coherence of multiple excitons in PbS/CdS core-shell nanocrystals, *Phys. Rev. Lett.*, 2017, **119**, 247401.
 82. O. E. Semonin, J. M. Luther, S. Choi, H.-Y. Chen, J. Gao, A. J. Nozik and M. C. Beard, Peak External Photocurrent Quantum Efficiency Exceeding 100% via MEG in a Quantum Dot Solar Cell, *Science*, 2011, **334**, 1530.
 83. H. Tahara, M. Sakamoto, T. Teranishi and Y. Kanemitsu, Collective enhancement of quantum coherence in coupled quantum dot films, *Phys. Rev. B*, 2021, **104**, L241405.
 84. V. I. Klimov, A. A. Mikhailovsky, D. W. McBranch, C. A. Leatherdale and M. G. Bawendi, Quantization of multiparticle Auger rates in semiconductor quantum dots, *Science*, 2000, **287**, 1011-1013.
 85. A. J. Nozik, M. C. Beard, J. M. Luther, M. Law, R. J. Ellingson and J. C. Johnson, Semiconductor quantum dots and quantum dot arrays and applications of multiple exciton generation to third-generation photovoltaic solar cells. *Chem. Rev.*, 2010, **110**, 6873-6890.
 86. J. M. Pietryga, Y. S. Park, J. Lim, A. F. Fidler, W. K. Bae, S. Brovelli and V. I. Klimov, Spectroscopic and device aspects of nanocrystal quantum dots, *Chem. Rev.*, 2016, **116**, 10513-10622.
 87. M. Nirmal, B. O. Dabbousi, M. G. Bawendi, J. J. Macklin, J. K. Trautman, T. D. Harris and L. E. Brus, Fluorescence intermittency in single cadmium selenide nanocrystals. *Nature*, 1996, **383**, 802-804.
 88. Al. L. Efros and M. Rosen. Random telegraph signal in the photoluminescence intensity of a single quantum dot, *Phys. Rev. Lett.*, 1997, **78**, 1110-1113.
 89. A. L. Efros and D. J. Nesbitt, Origin and control of blinking in quantum dots, *Nat. Nanotechnol.*, 2016, **11**, 661-671.
 90. J. Iveland, L. Martinelli, J. Peretti, J. S. Speck and C. Weisbuch, Direct measurement of Auger electrons emitted from a semiconductor light-emitting diode under electrical injection: identification of the dominant mechanism for efficiency droop, *Phys. Rev. Lett.*, 2013, **110**, 177406.
 91. Y. Shirasaki, G. J. Supran, M. G. Bawendi and V. Bulović, Emergence of colloidal quantum-dot light-emitting technologies, *Nat. Photonics*, 2013, **7**, 13-23.
 92. P. Michler, A. Imamoglu, M. D. Mason, P. J. Carson, G. F. Strouse and S. K. Buratto, Quantum correlation among photons from a single quantum dot at room temperature. *Nature*, 2000, **406**, 968-970 (2000).
 93. X. Brokmann, G. Messin, P. Desbiolles, E. Giacobino, M. Dahan and J. P. Hermier, Colloidal CdSe/ZnS quantum dots as single-photon sources, *New J. Phys.*, 2004, **6**, 99-99.
 94. Y.-S. Park, S. Guo, N. S. Makarov and V. I. Klimov, Room temperature single-photon emission from individual perovskite quantum dots, *ACS Nano*, 2015, **9**, 10386-10393.

95. C. Zhu, M. Marczak, L. Feld, S. C. Boehme, C. Bernasconi, A. Moskalenko, I. Cherniukh, D. Dirin, M. I. Bodnarchuk, M. V. Kovalenko and G. Rainò, Room-Temperature, Highly Pure Single-Photon Sources from All-Inorganic Lead Halide Perovskite Quantum Dots, *Nano Lett.*, 2022, **22**, 3751–3760.
96. T. Umebayashi, K. Asai, T. Kondo and A. Nakao, Electronic structures of lead iodide based low-dimensional crystals, *Phys. Rev. B*, 2003, **67**, 155405.
97. J. Even, L. Pedesseau, J.-M. Jancu and C. Katan, Importance of spin–orbit coupling in hybrid organic/inorganic perovskites for photovoltaic applications, *J. Phys. Chem. Lett.*, 2013, **4**, 2999-3005.
98. D. Giovanni, H. Ma, J. Chua, M. Grätzel, R. Ramesh, S. Mhaisalkar, N. Mathews and T. C. Sum, Highly spin-polarized carrier dynamics and ultralarge photoinduced magnetization in $\text{CH}_3\text{NH}_3\text{PbI}_3$ perovskite thin films, *Nano Lett.*, 2015, **15**, 1553-1558.
99. Z. G. Yu, Effective-mass model and magneto-optical properties in hybrid perovskites, *Sci. Rep.*, 2016, **6**, 28576.
100. M. A. Becker, R. Vaxenburg, G. Nedelcu, P. C. Sercel, A. Shabaev, M. J. Mehl, J. G. Michopoulos, S. G. Lambrakos, N. Bernstein, J. L. Lyons, T. Stöferle, R. F. Mahrt, M. V. Kovalenko, D. J. Norris, G. Rainò and A. L. Efros, Bright triplet excitons in caesium lead halide perovskites, *Nature*, 2018, **553**, 189-193.
101. G. Yumoto, H. Hirori, F. Sekiguchi, R. Sato, M. Saruyama, T. Teranishi and Y. Kanemitsu, Strong spin-orbit coupling inducing autler-townes effect in lead halide perovskite nanocrystals, *Nat. Commun.*, 2021, **12**, 3026.
102. T. Yamada, T. Aharen and Y. Kanemitsu, Near-band-edge optical responses of $\text{CH}_3\text{NH}_3\text{PbCl}_3$ single crystals: Photon recycling of excitonic luminescence, *Phys. Rev. Lett.*, 2018, **120**, 057404.
103. K. Ohara, T. Yamada, H. Tahara, T. Aharen, H. Hirori, H. Suzuura and Y. Kanemitsu, Excitonic enhancement of optical nonlinearities in perovskite $\text{CH}_3\text{NH}_3\text{PbI}_3$ single crystals, *Phys. Rev. Mater.*, 2019, **3**, 111601.
104. K. Ohara, T. Yamada, T. Aharen, H. Tahara, H. Hirori, H. Suzuura and Y. Kanemitsu, Impact of spin-orbit splitting on two-photon absorption spectra in a halide perovskite single crystal, *Phys. Rev. B*, 2021, **103**, L041201.
105. S. H. Autler and C. H. Townes, Stark effect in rapidly varying fields, *Phys. Rev.*, 1955, **100**, 703-722.
106. A. Von Lehmen, D. S. Chemla, J. E. Zucker and J. P. Heritage, Optical stark effect on excitons in GaAs quantum wells, *Opt. Lett.*, 1986, **11**, 609-611.
107. E. J. Sie, J. W. McIver, Y.-H. Lee, L. Fu, J. Kong and N. Gedik, Valley-selective optical stark effect in monolayer WS_2 , *Nat. Mater.*, 2015, **14**, 290-294.
108. D. Giovanni, W. K. Chong, H. A. Dewi, K. Thirumal, I. Neogi, R. Ramesh, S. Mhaisalkar, N. Mathews and T. C. Sum, Tunable room-temperature spin-selective optical stark effect in solution-processed layered halide perovskites, *Sci. Adv.*, 2016, **2**, e1600477.
109. Y. Yang, M. Yang, K. Zhu, J. C. Johnson, J. J. Berry, J. van de Lagemaat and M. C. Beard, Large polarization-dependent exciton optical stark effect in lead iodide perovskites, *Nat. Commun.*, 2016, **7**, 12613.
110. K. Wu, Y. S. Park, J. Lim and V. I. Klimov, Towards zero-threshold optical gain using charged semiconductor quantum dots, *Nat. Nanotech.*, 2017, **12**, 1140-1147.
111. F. Hu, H. Zhang, C. Sun, C. Yin, B. Lv, C. Zhang, W. Yu, X. Wang, Y. Zhang, M. Xiao, Superior Optical

- Properties of Perovskite Nanocrystals as Single Photon Emitters. *ACS Nano*, 2015, **9**, 12410–12416.
112. F. Zheng, L. Z. Tan, S. Liu and A. M. Rappe, Rashba spin–orbit coupling enhanced carrier lifetime in $\text{CH}_3\text{NH}_3\text{PbI}_3$, *Nano Lett.*, 2015, **15**, 7794–7800.
113. L. Z. Tan, F. Zheng, S. M. Young, F. Wang, S. Liu and A. M. Rappe, Shift current bulk photovoltaic effect in polar materials-hybrid and oxide perovskites and beyond, *npj Comput. Mater.*, 2016, **2**, 16026.
114. M. Isarov, L. Z. Tan, M. I. Bodnarchuk, M. V. Kovalenko, A. M. Rappe and E. Lifshitz, Rashba effect in a single colloidal CsPbBr_3 perovskite nanocrystal detected by magneto-optical measurements. *Nano Lett.*, 2017, **17**, 5020–5026.
115. D. Niesner, M. Hauck, S. Shrestha, I. Levchuk, G. J. Matt, A. Osvet, M. Batentschuk, C. Brabec, H. B. Weber and T. Fauster, Structural fluctuations cause spin-split states in tetragonal $(\text{CH}_3\text{NH}_3)\text{PbI}_3$ as evidenced by the circular photogalvanic effect, *Proc. Natl. Acad. Sci.*, 2018, **115**, 9509–9514.
116. K. Frohna, T. Deshpande, J. Harter, W. Peng, B. A. Barker, J. B. Neaton, S. G. Louie, O. M. Bakr, D. Hsieh and M. Bernardi, Inversion symmetry and bulk Rashba effect in methylammonium lead iodide perovskite single crystals. *Nat. Commun.*, 2018, **9**, 1829.
117. Y. Ogawa, H. Tahara, N. Igarashi, Y. Yamada and Y. Kanemitsu, Spectral characterization of the Rashba spin-split band in a lead halide perovskite single crystal by photocurrent heterodyne interference spectroscopy, *Phys. Rev. B*, 2021, **103**, L081201.
118. E. Lafalce, E. Amerling, Z.-G. Yu, P. C. Sercel, L. Whittaker-Brooks and Z. V. Vardeny, Rashba splitting in organic–inorganic lead–halide perovskites revealed through two-photon absorption spectroscopy, *Nature Commun.*, 2022, **13**, 483.
119. P. C. Sercel, J. L. Lyons, D. Wickramaratne, R. Vaxenburg, N. Bernstein and A. L. Efros, Exciton fine structure in perovskite nanocrystals, *Nano Lett.*, 2019, **19**, 4068–4077.
120. P. Tamarat, M. I. Bodnarchuk, J. B. Trebbia, R. Erni, M. V. Kovalenko, J. Even and B. Lounis, The ground exciton state of formamidinium lead bromide perovskite nanocrystals is a singlet dark state, *Nat. Mater.*, 2019, **18**, 717–724.
121. P. Tamarat, L. Hou, J.-B. Trebbia, A. Swarnkar, L. Biadala, Y. Louyer, M. I. Bodnarchuk, M. V. Kovalenko, J. Even and B. Lounis, The dark exciton ground state promotes photon-pair emission in individual perovskite nanocrystals, *Nature Commun.*, 2020, **11**, 6001.
122. C. Yin, L. Chen, N. Song, Y. Lv, F. Hu, C. Sun, W. W. Yu, C. Zhang, X. Wang, Y. Zhang and M. Xiao, Bright-Exciton Fine-Structure Splittings in Single Perovskite Nanocrystals, *Phys. Rev. Lett.*, 2017, **119**, 026401.
123. M. Fu, P. Tamarat, H. Huang, J. Even, A. L. Rogach and B. Lounis, Neutral and Charged Exciton Fine Structure in Single Lead Halide Perovskite Nanocrystals Revealed by Magneto-optical Spectroscopy, *Nano Lett.*, 2017, **17**, 2895–2901.
124. K. Cho, H. Tahara, T. Yamada, H. Suzuura, T. Tadano, R. Sato, M. Saruyama, H. Hirori, T. Teranishi and Y. Kanemitsu, Submitted for publication.
125. A. L. Efros and A. L. Efros, Interband Absorption of Light in Semiconductor Sphere. *Sov. Phys. Semicond.*, 1982, **16**, 772–775.

126. L. E. Brus, Electron-Electron and Electron-Hole Interactions in Small Semiconductor Crystallites: The Size Dependence of the Lowest Excited Electronic State, *J. Chem. Phys.*, 1984, **80**, 4403–4409.
127. Y. Kayanuma, Quantum-size effects of interacting electrons and holes in semiconductor microcrystals with spherical shape, *Phys. Rev. B*, 1988, **38**, 9797.
128. A. L. Efros, M. Rosen, M. Kuno, M. Nirmal, D. J. Norris and M. Bawendi, Band-edge exciton in quantum dots of semiconductors with a degenerate valence band: Dark and bright exciton states. *Phys. Rev. B*, 1996, **54**, 4843.
129. S. A. Empedocles and M. G. Bawendi, Quantum-confined stark effect in single CdSe nanocrystallite quantum dots, *Science*, 1997, **278**, 2114-2117.
130. T. Itoh, M. Furumiya, T. Ikehara, and C. Gourdon, Size-dependent radiative decay time of confined excitons in CuCl microcrystals, *Solid State Commun.*, 1990, **73**, 271-274.
131. Y. Masumoto, S. Okamoto, and S. Katayanagi, Biexciton binding energy in CuCl quantum dots. *Phys. Rev. B*, 1994, **50**, 18658.
132. P. C. Sercel, J. L. Lyons, N. Bernstein and Al. L. Efros, Quasicubic model for metal halide perovskite nanocrystals, *J. Chem. Phys.*, 2019, **151**, 234106.
133. M. C. Brennan, J. E. Herr, T. S. Nguyen-Beck, J. Zinna, S. Draguta, S. Rouvimov, J. Parkhill and M. Kuno, Origin of the size-dependent stokes shift in CsPbBr₃ perovskite nanocrystals, *J. Am. Chem. Soc.*, 2017, **139**, 12201-12208.
134. K. Cho, T. Yamada, H. Tahara, T. Tadano, H. Suzuura, M. Saruyama, R. Sato, T. Teranishi, and Y. Kanemitsu, Luminescence Fine Structures in Single Lead Halide Perovskite Nanocrystals: Size Dependence of the Exciton–Phonon Coupling. *Nano Lett.*, 2021, **21**, 7206-7212.
135. L. N. Quan, R. Quintero-Bermudez, O. Voznyy, G. Walters, A. Jain, J. Z. Fan, X. L. Zheng, Z. Y. Yang and E. H. Sargent, Highly emissive green perovskite nanocrystals in a solid state crystalline matrix, *Adv. Mater.*, 2017, **29**, 1605945.
136. X. Chen, F. Zhang, Y. Ge, L. Shi, S. Huang, J. Tang, Z. Lv, L. Zhang, B. Zou, and H. Zhong, Centimeter-sized Cs₄PbBr₆ crystals with embedded CsPbBr₃ nanocrystals showing superior photoluminescence: nonstoichiometry induced transformation and light-emitting applications, *Adv. Funct. Mater.*, **28**, 1706567 (2018).
137. Y. Kajino, S. Otake, T. Yamada, K. Kojima, T. Nakamura, A. Wakamiya, Y. Kanemitsu and Y. Yamada, Anti-stokes photoluminescence from CsPbBr₃ nanostructures embedded in a Cs₄PbBr₆ crystal, *Phys. Rev. Mater.*, 2022, **6**, L043001.
138. N. S. Makarov, S. Guo, O. Isaienko, W. Liu, I. Robel and V. I. Klimov, Spectral and dynamical properties of single excitons, biexcitons, and trions in cesium–lead-halide perovskite quantum dots, *Nano Lett.*, 2016, **16**, 2349-2362.
139. N. Yarita, H. Tahara, T. Ihara, T. Kawawaki, R. Sato, M. Saruyama, T. Teranishi and Y. Kanemitsu, Dynamics of charged excitons and biexcitons in CsPbBr₃ perovskite nanocrystals revealed by femtosecond transient-absorption and single-dot luminescence spectroscopy, *J. Phys. Chem. Lett.*, 2017, **8**, 1413-1418.
140. N. Yarita, T. Aharen, H. Tahara, M. Saruyama, T. Kawawaki, R. Sato, T. Teranishi and Y. Kanemitsu,

- Observation of positive and negative trions in organic-inorganic hybrid perovskite nanocrystals, *Phys. Rev. Mater.*, 2018, **2**, 116003.
141. N. Yarita, H. Tahara, M. Saruyama, T. Kawawaki, R. Sato, T. Teranishi and Y. Kanemitsu, Impact of postsynthetic surface modification on photoluminescence intermittency in formamidinium lead bromide perovskite nanocrystals, *J. Phys. Chem. Lett.*, 2017, **8**, 6041-6047.
142. S. Nakahara, H. Tahara, G. Yumoto, T. Kawawaki, M. Saruyama, R. Sato, T. Teranishi and Y. Kanemitsu, Suppression of trion formation in CsPbBr₃ perovskite nanocrystals by postsynthetic surface modification, *J. Phys. Chem. C*, 2018, **122**, 22188-22193.
143. S. Nakahara, K. Ohara, H. Tahara, G. Yumoto, T. Kawawaki, M. Saruyama, R. Sato, T. Teranishi and Y. Kanemitsu, Ionization and neutralization dynamics of CsPbBr₃ perovskite nanocrystals revealed by double-pump transient absorption spectroscopy, *J. Phys. Chem. Lett.*, 2019, **10**, 4731-4736.
144. W. Gao, J. Ding, Z. Bai, Y. Qi, Y. Wang and Z. Lv, Multiple excitons dynamics of lead halide perovskite, *Nanophotonics*, 2021, **10**, 3945-3955.
145. S. Masada, T. Yamada, H. Tahara, H. Hirori, M. Saruyama, T. Kawawaki, R. Sato, T. Teranishi and Y. Kanemitsu, Effect of A-site cation on photoluminescence spectra of single lead bromide perovskite nanocrystals, *Nano Lett.*, 2020, **20**, 4022-4028.
146. G. Nair, J. Zhao and M. G. Bawendi, Biexciton quantum yield of single semiconductor nanocrystals from photon statistics, *Nano Lett.*, 2011, **11**, 1136-1140.
147. N. Hiroshige, T. Ihara and Y. Kanemitsu, Simultaneously measured photoluminescence lifetime and quantum yield of two-photon cascade emission on single CdSe/ZnS nanocrystals. *Phys. Rev. B*, 2017, **95**, 245307.
148. N. Hiroshige, T. Ihara, M. Saruyama, T. Teranishi and Y. Kanemitsu, Coulomb-enhanced radiative recombination of biexcitons in single giant-shell CdSe/CdS core/shell nanocrystals. *J. Phys. Chem. Lett.*, 2017, **8**, 1961-1966.
149. Y.-S. Park, W. K. Bae, J. M. Pietryga and V. I. Klimov, Auger recombination of biexcitons and negative and positive trions in individual quantum dots, *ACS Nano*, 2014, **8**, 7288-7296.
150. C. Galland, Y. Ghosh, A. Steinbrück, M. Sykora, J. A. Hollingsworth, V. I. Klimov, H. Htoon, Two Types of Luminescence Blinking Revealed by Spectroelectrochemistry of Single Quantum Dots, *Nature*, 2011, **479**, 203-207.
151. C. T. Trinh, D. N. Minh, K. J. Ahn, Y. Kang and K. G. Lee, Verification of Type-A and Type-B-HC Blinking Mechanisms of Organic-Inorganic Formamidinium Lead Halide Perovskite Quantum Dots by FLID Measurements. *Sci. Rep.*, 2020, **10**, 2172.
152. F. Zhu, L. Men, Y. Guo, Q. Zhu, U. Bhattacharjee, P. M. Goodwin, J. W. Petrich, E. A. Smith and J. Vela, Shape Evolution and Single Particle Luminescence of Organometal Halide Perovskite Nanocrystals, *ACS Nano*, 2015, **9**, 2948-2959.
153. Y. Tian, A. Merdasa, M. Peter, M. Abdellah, K. Zheng, C. S. Ponseca, Jr., T. Pullerits, A. Yartsev, V. Sundström and I. G. Scheblykin, Giant Photoluminescence Blinking of Perovskite Nanocrystals Reveals Single-Trap Control of Luminescence, *Nano Lett.*, 2015, **15**, 1603-1608.
154. X. Wen, A. Ho-Baillie, S. Huang, R. Sheng, S. Chen, H.-C. Ko and M. A. Green, Mobile Charge-Induced

- Fluorescence Intermittency in Methylammonium Lead Bromide Perovskite, *Nano Lett.*, 2015, **15**, 4644–4649.
155. J. Wang, T. Ding, J. Leng, S. Jin and K. Wu, Intact Carrier Doping by Pump–Pump–Probe Spectroscopy in Combination with Interfacial Charge Transfer: A Case Study of CsPbBr₃ Nanocrystals, *J. Phys. Chem. Lett.*, 2018, **9**, 3372–3377.
156. Y.-S. Park, W. K. Bae, L. A. Padilha, J. M. Pietryga and V. I. Klimov, Effect of the core/shell interface on Auger recombination evaluated by single-quantum-dot spectroscopy, *Nano Lett.*, 2014, **14**, 396–402.
157. W. K. Bae, L. A. Padilha, Y. -S. Park, H. McDaniel, I. Robel, J. M. Pietryga and V. I. Klimov, Controlled alloying of the core–shell interface in CdSe/CdS quantum dots for suppression of Auger recombination, *ACS Nano*, 2013, **7**, 3411–3419.
158. M. Nasilowski, P. Spinicelli, G. Patriarche and B. Dubertret, Gradient CdSe/CdS quantum dots with room temperature biexciton unity quantum yield, *Nano Lett.*, 2015, **15**, 3953–3958.
159. K. E. Shulenberger, M. N. Ashner, S. K. Ha, F. Krieg, M. V. Kovalenko, W. A. Tisdale and M. G. Bawendi, (2019). Setting an upper bound to the biexciton binding energy in CsPbBr₃ perovskite nanocrystals, *J. Phys. Chem. Lett.*, 2019, **10**, 5680–5686.
160. J. Aneesh, A. Swarnkar, V. Kumar Ravi, R. Sharma, A. Nag and K. V. Adarsh, Ultrafast exciton dynamics in colloidal CsPbBr₃ perovskite nanocrystals: Biexciton effect and Auger recombination, *J. Phys. Chem. C*, 2017, **121**, 4734–4739.
161. X. Shen, S. Wang, C. Geng, L. Li, E. Zhao, J. Sun, W. Wu, L. An and K. Pan, Red shift of bleaching signals in femtosecond transient absorption spectra of CsPbX₃ (X = Cl/Br, Br, Br/I) nanocrystals induced by the biexciton effect, *J. Phys. Chem. C*, 2021, **125**, 5278–5287.
162. G. Lubin, G. Yaniv, M. Kazes, A. C. Ulku, I. M. Antolovic, S. Burri, C. Bruschini, E. Charbon, V. J. Yallapragada and D. Oron, Resolving the controversy in biexciton binding energy of cesium lead halide perovskite nanocrystals through heralded single-particle spectroscopy, *ACS Nano*, 2021, **15**, 19581–19587.
163. M. N. Ashner, K. E. Shulenberger, F. Krieg, E. R. Powers, M. V. Kovalenko, M. G. Bawendi and W. A. Tisdale, Size-dependent biexciton spectrum in CsPbBr₃ perovskite nanocrystals, *ACS Energy Lett.*, 2019, **4**, 2639–2645.
164. M. Achermann, J. A. Hollingsworth and V. I. Klimov, Multiexcitons confined within a subexcitonic volume: Spectroscopic and dynamical signatures of neutral and charged biexcitons in ultrasmall semiconductor nanocrystals, *Phys. Rev. B*, 2003, **68**, 245302.
165. T. Takagahara, Biexciton states in semiconductor quantum dots and their nonlinear optical properties, *Phys. Rev. B*, 1989, **39**, 10206.
166. H. Zhu, K. Miyata, Y. Fu, J. Wang, P. P. Joshi, D. Niesner, K. W. Williams, S. Jin and X.-Y. Zhu, Screening in crystalline liquids protects energetic carriers in hybrid perovskites, *Science*, 2016, **353**, 1409–1413.
167. Y. Yang, D. P. Ostrowski, R. M. France, K. Zhu, J. van de Lagemaat, J. M. Luther and M. C. Beard, Observation of a hot-phonon bottleneck in lead-iodide perovskites, *Nat. Photonics*, 2016, **10**, 53–59.
168. M. B. Price, J. Butkus, T. C. Jellicoe, A. Sadhanala, A. Briane, J. E. Halpert, K. Broch, J. M. Hodgkiss, R. H. Friend and F. Deschler, Hot-carrier cooling and photoinduced refractive index changes in organic–inorganic lead halide perovskites, *Nat. Commun.*, 2015, **6**, 8420.

169. M. Li, S. Bhaumik, T. W. Goh, M. S. Kumar, N. Yantara, M. Graetzel, S. Mhaisalkar, N. Mathews and T. C. Sum, Slow cooling and highly efficient extraction of hot carriers in colloidal perovskite nanocrystals, *Nat. Commun.*, 2017, **8**, 14350.
170. J. Fu, Q. Xu, G. Han, B. Wu, C. H. A. Huan, M. L. Leek and T. C. Sum, Hot carrier cooling mechanisms in halide perovskites, *Nat. Commun.*, 2017, **8**, 1300.
171. J. Yang, X. Wen, H. Xia, R. Sheng, Q. Ma, J. Kim, P. Tapping, T. Harada, T. W. Kee, F. Huang, Y.-B. Cheng, M. Green, A. Ho-Baillie, S. Huang, S. Shrestha, R. Patterson and G. Conibeer, Acoustic-optical phonon up-conversion and hot-phonon bottleneck in lead-halide perovskites, *Nat. Commun.*, 2017, **8**, 14120.
172. Q. Shen, T. S. Ripolles, J. Even, Y. Ogomi, K. Nishinaka, T. Izuishi, N. Nakazawa, Y. Zhang, C. Ding, F. Liu, T. Toyoda, K. Yoshino, T. Minemoto, K. Katayama and S. Hayase, Slow hot carrier cooling in cesium lead iodide perovskites, *Appl. Phys. Lett.*, 2017, **111**, 153903.
173. F. Sekiguchi, H. Hirori, G. Yumoto, A. Shimazaki, T. Nakamura, A. Wakamiya and Y. Kanemitsu, Enhancing the Hot-Phonon Bottleneck Effect in a Metal Halide Perovskite by Terahertz Phonon Excitation, *Phys. Rev. Lett.*, 2021, **126**, 077401.
174. J. Shah, *Hot carriers in semiconductor nanostructures: Physics and applications*, Academic Press, Inc.: San Diego, CA, 1992.
175. J. A. Kash, J. C. Tsang and J. M. Hvam, Subpicosecond time-resolved Raman spectroscopy of LO phonons in GaAs, *Phys. Rev. Lett.*, 1985, **54**, 2151.
176. H. Utzat, W. Sun, A. E. K. Kaplan, F. Krieg, M. Ginterseder, B. Spokoyny, N. D. Klein, K. E. Shulenberger, C. F. Perkinson, M. V. Kovalenko and M. G. Bawendi, Coherent single-photon emission from colloidal lead halide perovskite quantum dots, *Science*, 2019, **363**, 1068-1072.
177. C. Santori, D. Fattal, M. Pelton, G. S. Solomon and Y. Yamamoto, Polarization-correlated photon pairs from a single quantum dot, *Phys. Rev. B*, 2002, **66**, 045308.
178. A. Muller, W. Fang, J. Lawall and G. S. Solomon, Creating polarization-entangled photon pairs from a semiconductor quantum dot using the optical stark effect, *Phys. Rev. Lett.*, 2009, **103**, 217402.
179. R. M. Stevenson, R. J. Young, P. Atkinson, K. Cooper, D. A. Ritchie and A. J. Shields, A semiconductor source of triggered entangled photon pairs, *Nature*, 2006, **439**, 179-182.
180. J. E. Avron, G. Bisker, D. Gershoni, N. H. Lindner, E. A. Meirom and R. J. Warburton, Entanglement on demand through time reordering, *Phys. Rev. Lett.*, 2008, **100**, 120501.
181. J. D. Plumhof, R. Trotta, A. Rastelli and O. G. Schmidt, Experimental methods of post-growth tuning of the excitonic fine structure splitting in semiconductor quantum dots, *Nanoscale Res. Lett.*, 2012, **7**, 336.
182. F. Ding, R. Singh, J. D. Plumhof, T. Zander, V. Krápek, Y. H. Chen, M. Benyoucef, V. Zwiller, K. Dörr, G. Bester, A. Rastelli and O. G. Schmidt, Tuning the exciton binding energies in single self-assembled InGaAs/GaAs quantum dots by piezoelectric-induced biaxial stress, *Phys. Rev. Lett.*, 2010, **104**, 067405.
183. P. Tyagi, S. M. Arveson and W. A. Tisdale, Colloidal organohalide perovskite nanoplatelets exhibiting quantum confinement, *J. Phys. Chem. Lett.*, 2015, **6**, 1911-1916.
184. Y. Tong, F. Ehrat, W. Vanderlinden, C. Cardenas-Daw, J. K. Stolarczyk, L. Polavarapu and A. S. Urban, Dilution-Induced Formation of Hybrid Perovskite Nanoplatelets, *ACS Nano*, 2016, **10**, 10936-10944.

185. L. Dou, A. B. Wong, Y. Yu, M. Lai, N. Kornienko, S. W. Eaton, A. Fu, C. G. Bischak, J. Ma, T. Ding, N. S. Ginsberg, L.-W. Wang, A. P. Alivisatos and P. Yang, Atomically thin two-dimensional organic-inorganic hybrid perovskites, *Science*, 2015, **349**, 1518-1521.
186. Y. Chen, Y. Sun, J. Peng, J. Tang, K. Zheng and Z. Liang, 2D Ruddlesden–Popper perovskites for optoelectronics, *Adv. Mater.*, 2018, **30**, 1703487.
187. J.-C. Blancon, J. Even, C. C. Stoumpos, M. G. Kanatzidis and A. D. Mohite, Semiconductor physics of organic–inorganic 2D halide perovskites, *Nat. Nanotechnol.*, 2020, **15**, 969-985.
188. J.-C. Blancon, A. V. Stier, H. Tsai, W. Nie, C. C. Stoumpos, B. Traoré, L. Pedesseau, M. Kepenekian, F. Katsutani, G. T. Noe, J. Kono, S. Tretiak, S. A. Crooker, C. Katan, M. G. Kanatzidis, J. J. Crochet, J. Even and A. D. Mohite, Scaling law for excitons in 2D perovskite quantum wells, *Nature Commun.*, 2018, **9**, 2254.
189. H. Lu, J. Wang, C. Xiao, X. Pan, X. Chen, R. Brunecky, J. J. Berry, K. Zhu, M. C. Beard and Z. V. Vardeny, Spin-dependent charge transport through 2D chiral hybrid lead-iodide perovskites, *Sci. Adv.*, 2019, **5**, eaay0571.
190. G. Yumoto, F. Sekiguchi, R. Hashimoto, T. Nakamura, A. Wakamiya and Y. Kanemitsu, *Sci. Adv.*, 2022, **8**, eabp8135.
191. P. Siwach, P. Sikarwar, J. S. Halpati and A. K. Chandiran, Design of above-room-temperature ferroelectric two-dimensional layered halide perovskites, *J. Mater. Chem. A*, 2022, **10**, 8719-8738.
192. H.-Y. Ye, Y.-Y. Tang, P.-F. Li, W.-Q. Liao, J.-X. Gao, X.-N. Hua, H. Cai, P.-P. Shi, Y.-M. You and R.-G. Xiong, Metal-free three-dimensional perovskite ferroelectrics, *Science*, 2018, **361**, 151–155.
193. T. Handa, R. Hashimoto, G. Yumoto, T. Nakamura, A. Wakamiya and Y. Kanemitsu, Metal-free ferroelectric halide perovskite exhibits visible photoluminescence correlated with local ferroelectricity, *Sci. Adv.*, 2022, **8**, eabo1621.

Acknowledgements

The authors would like to thank H. Tahara, N. Yarita, T. Handa, T. Yamada, S. Nakahara, K. Ohara, N. Hiroshige, K. Cho, E. Kobiyama, H. Hirori, F. Sekiguchi, T. Tadano, H. Suzuura, M. Saruyama, T. Kawawaki, R. Sato, and T. Teranishi for collaboration, help with the experiments, and discussions. Part of this work was supported by JSPS KAKENHI (Grant No. JP19H05465) and JST CREST (Grant Nos. JPMJCR16N3 and JPMJCR21B4).

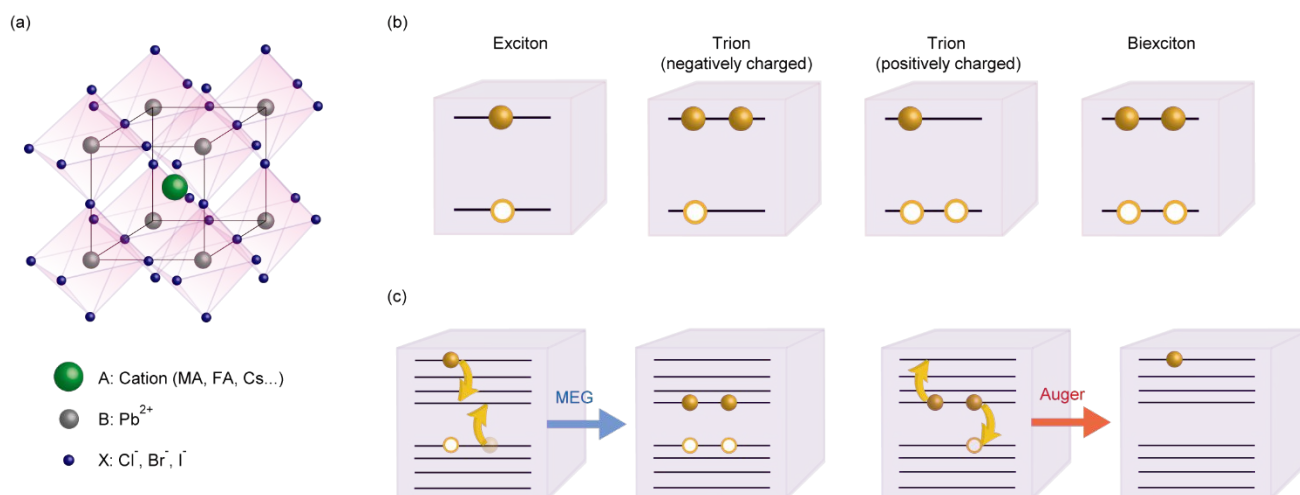


Fig. 1 (a) Crystal structure of lead halide perovskites APbX_3 . (b) Illustration of exciton and multiexciton states, which determine the optical responses of lead halide perovskite nanocrystals. Solid (open) circles represent electrons (holes). (c) Schematics of multiple exciton generation (MEG) and Auger recombination processes.

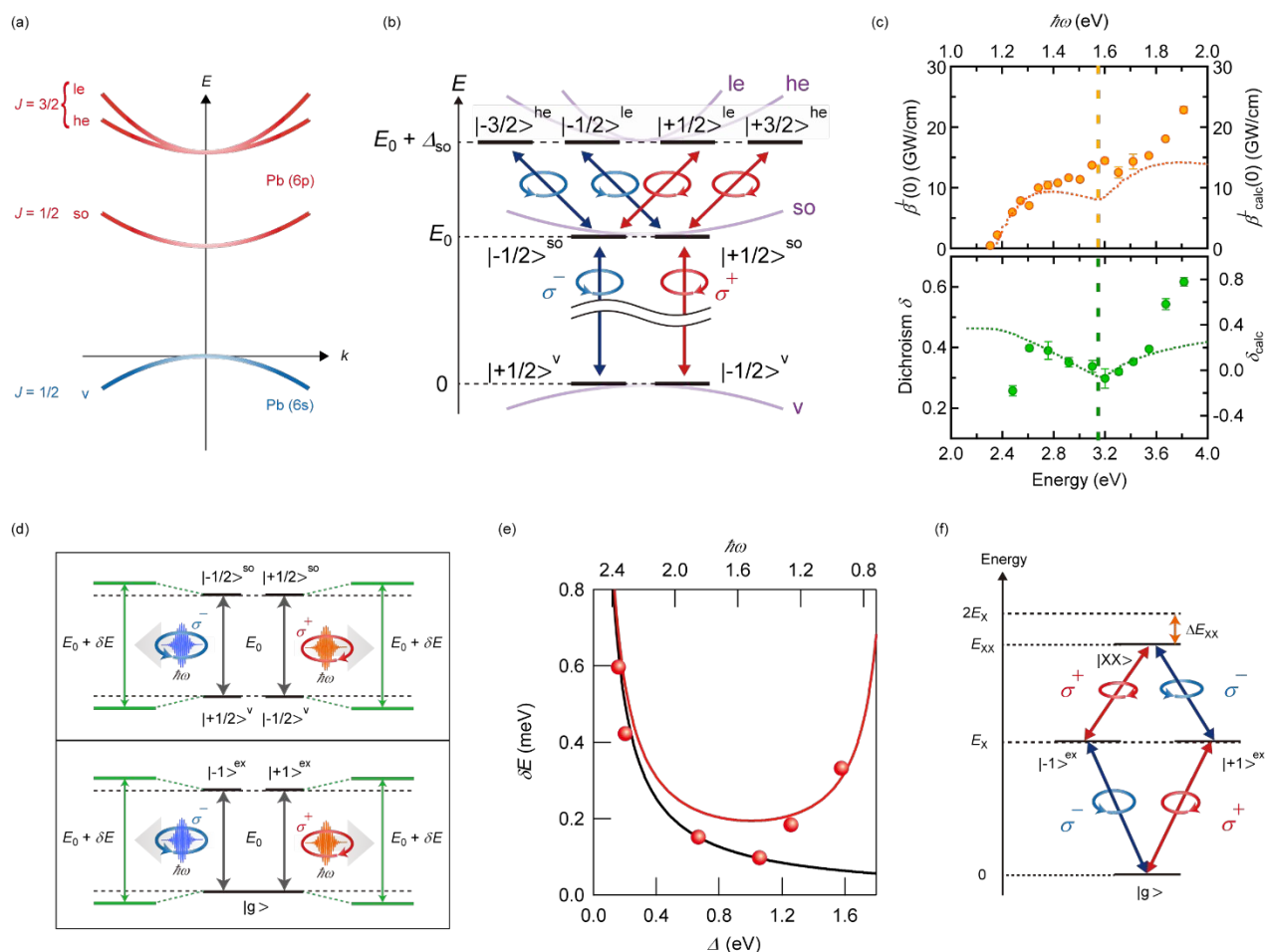


Fig. 2 (a) Electronic band structure of lead halide perovskites. le , light-electron conduction band; he , heavy-electron conduction band; so , split-off conduction band; v , valence band. (b) Optical transition selection rules between band-edge states and between conduction band states. Δ_{so} denotes the spin-orbit splitting energy. (c) Excitation energy dependences of two-photon absorption coefficient (top panel) and dichroism (bottom panel). The top and bottom axes are the excitation energy $\hbar\omega$ and twice of that $2\hbar\omega$, respectively. The dotted curves are theoretical results. The vertical dashed lines represent the lowest energy of the heavy- and light-electron bands. (d) Schematics of the two-level optical Stark effect in lead halide perovskites. The upper panel shows that when the band-edge optical transition from $|-1/2\rangle^v$ to $|+1/2\rangle^{so}$ (from $|+1/2\rangle^v$ to $|-1/2\rangle^{so}$) is driven by right- (left-) handed circularly polarized laser pulse, the energy spacing between the two states shifts from E_0 to $E_0 + \delta E$ only during the laser excitation. The lower panel is the corresponding description with the exciton picture. (e) Pump energy dependence of the energy shift for σ^+ -pump and σ^+ -probe pulses, observed in $CsPbBr_3$ nanocrystals. The top and bottom axes are the pump energy $\hbar\omega$ and the pump detuning energy defined as $E_0 - \hbar\omega$, respectively. The red and black curves show the calculated energy shift based on the Autler–Townes effect and the two-level optical Stark effect, respectively. (f) Energy level diagram and optical transition selection rules for exciton ($|\pm 1\rangle^{ex}$) and biexciton ($|\pm XX\rangle$) states. Panels (b) and (e) are reproduced from ref. 101. Copyright 2021, The Authors, Published by Springer Nature under the Creative Commons Attribution 4.0 International license. Panel (c) is reproduced with permission from ref. 104. Copyright 2021, American Physical Society.

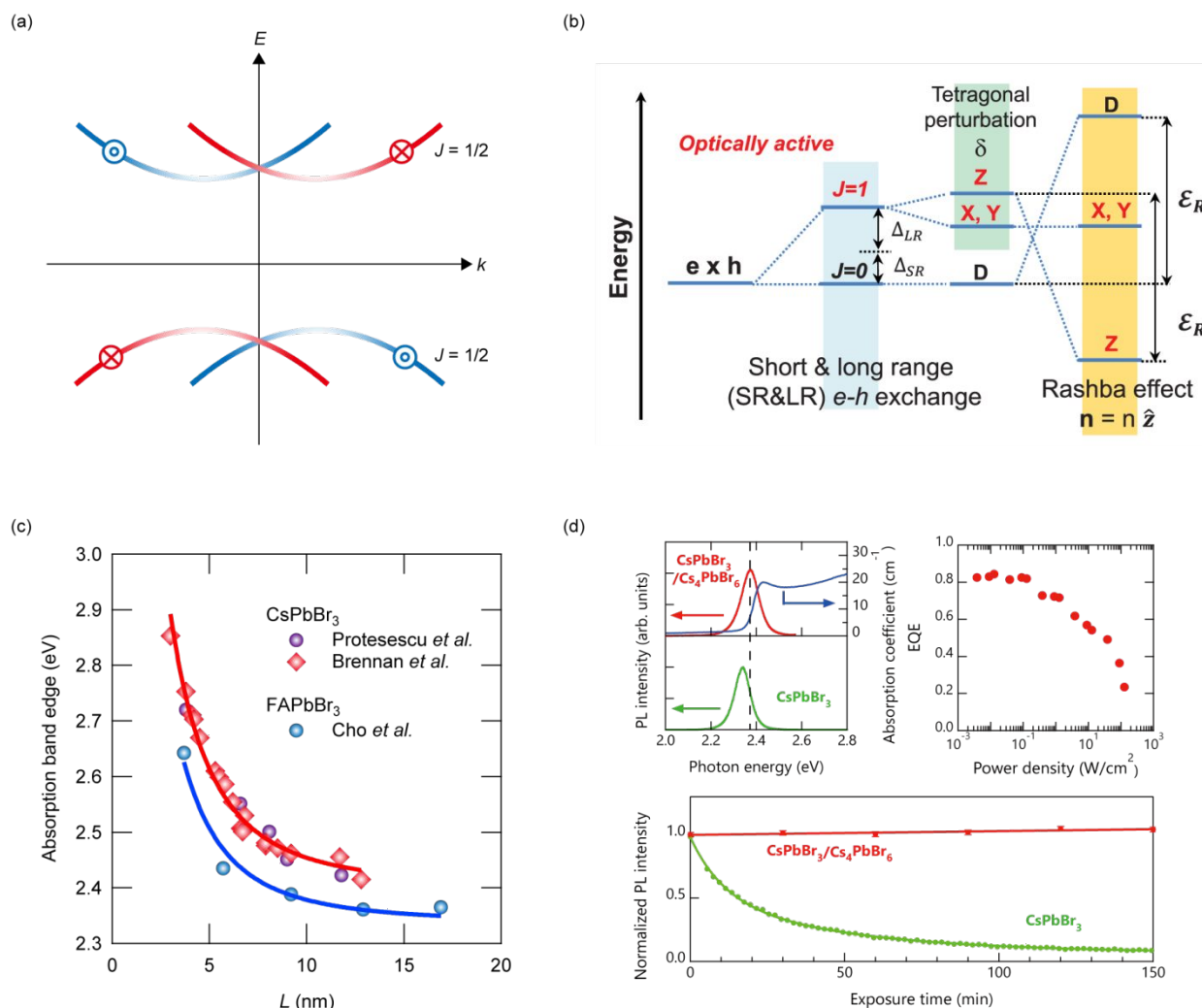


Fig. 3 (a) Rashba spin-split band structure in lead halide perovskites. (b) Schematic for how the Rashba effect modifies the energy structure of exciton states in lead halide perovskite nanocrystals. (c) The size dependence of the absorption band edge energy in lead halide perovskite nanocrystals. Data are taken from refs. 53, 133, and 134. The solid curves are calculated results based on ref. 132. (d) Top left: Optical absorption and PL spectra of $\text{CsPbBr}_3/\text{Cs}_4\text{PbBr}_6$ (upper panel) and CsPbBr_3 bulk crystals (lower panel). Top right: Dependence of the external quantum efficiency on the excitation power density for the $\text{CsPbBr}_3/\text{Cs}_4\text{PbBr}_6$ crystal. Excitation photon energy was 3.1 eV. Bottom: Stability of the PL intensity against light exposure for the $\text{CsPbBr}_3/\text{Cs}_4\text{PbBr}_6$ (red data) and the CsPbBr_3 bulk crystal (green data) under continuous-wave photoexcitation in air at room temperature. Panel (b) is adopted with permission from ref. 119. Copyright 2019, American Chemical Society. Panel (d) is adopted with permission from ref. 137. Copyright 2022, American Physical Society.

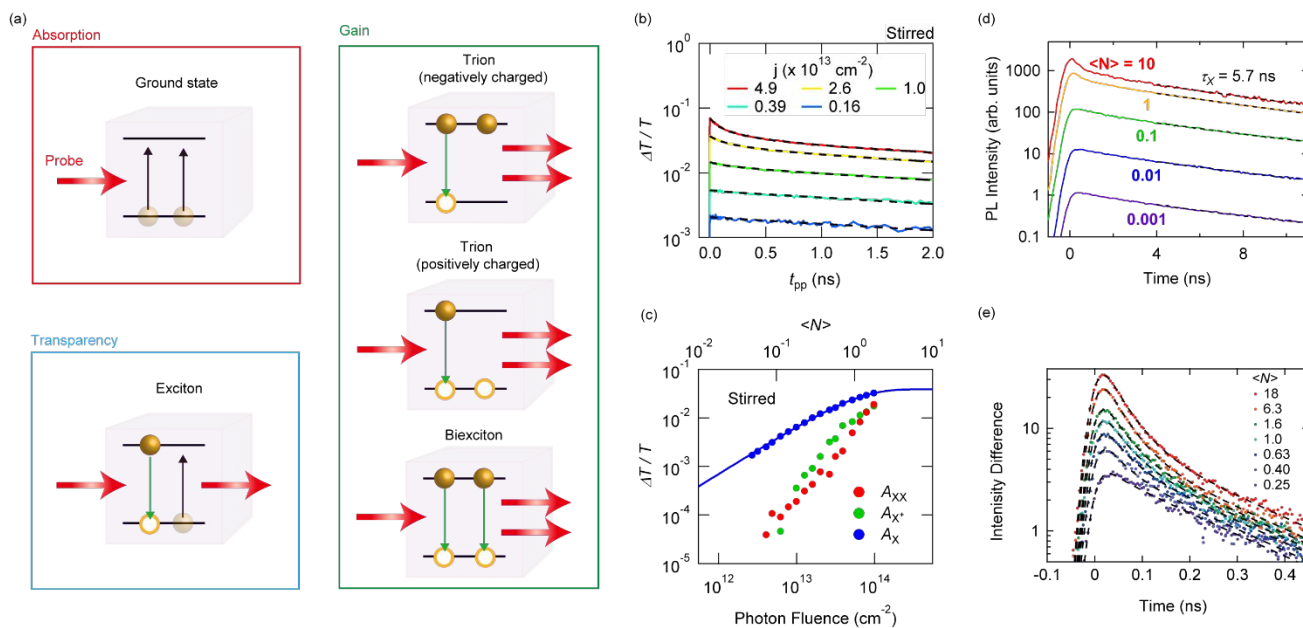


Fig. 4 (a) Schematics of how the photoexcited states determine the transmission of the probe pulse with photon energies around the band edge. The green and black arrows represent stimulated emission and absorption, respectively. When stimulated emission overcomes absorption, the probe light is amplified and optical gain appears. (b) Dynamics of the pump-induced change in transmission for various excitation fluences in CsPbBr₃ nanocrystals. The dashed curves are the global fitting results using the triple exponential function. (c) Pump photon fluence dependence of estimated amplitudes of the exciton (A_X), trion (A_{X^+}), and biexciton (A_{XX}). The solid curve shows the fitting result using the Poisson distribution. (d,e) PL dynamics (d) and fast-decay components of the PL curves (e) of CsPbBr₃ nanocrystals for different excitation fluences. Panel (b) is adopted and panel (c) is reproduced with permission from ref. 142. Copyright 2018, American Chemical Society. Panels (d) and (e) are adopted with permission from ref. 139. Copyright 2017, American Chemical Society.

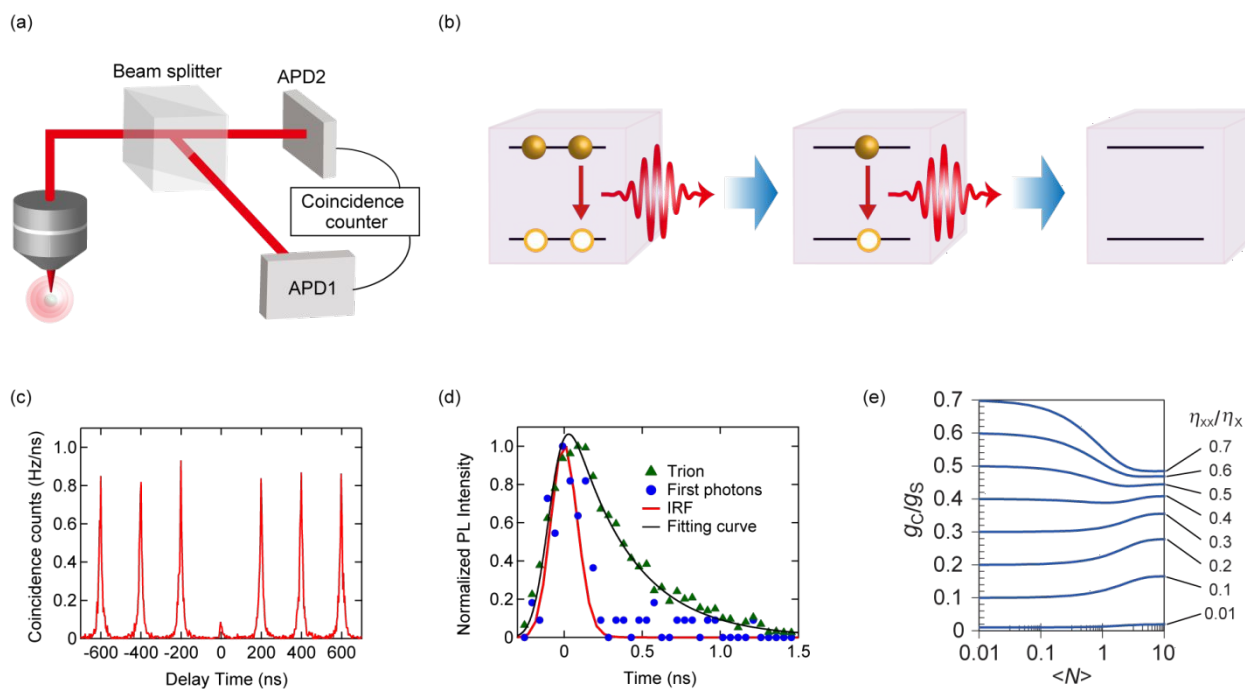


Fig. 5 (a) Schematic of a Hanbury–Brown–Twiss interferometer. APD denotes avalanche photodiode. (b) Illustration of the biexciton–exciton cascade emission. (c,d) Second-order correlation function (c) and PL dynamics of trion and first photons (d) observed for a single CsPbBr₃ nanocrystal. IRF denotes instrument response function. (e) Calculated $\langle N \rangle$ dependence of g_c/g_s for different values of η_{xx}/η_x . Panels (c) and (d) are adopted with permission from ref. 139. Copyright 2017, American Chemical Society. Panel (e) is adopted with permission from ref. 147. Copyright 2017, American Physical Society.

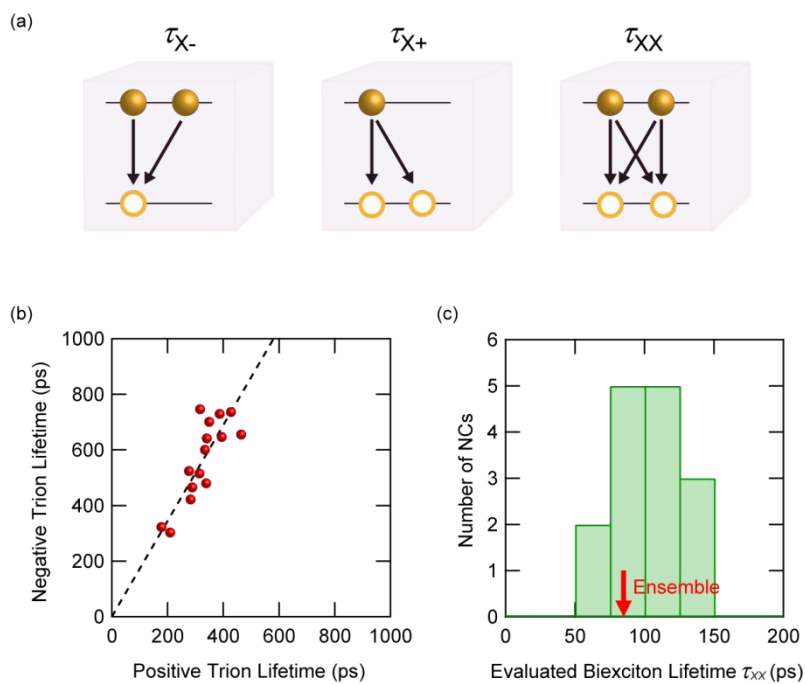


Fig. 6 (a) Schematics of recombination pathways in negative and positive trions, and biexciton. (b) Relationship between the negative and positive trion lifetimes in FAPbBr₃ nanocrystals. The dashed line is a linear fit. (c) Histogram of the biexciton lifetime estimated from the lifetimes of negative and positive trions. The red arrow indicates the biexciton lifetime of the ensemble nanocrystals obtained from transient absorption measurements. Panels (b) and (c) are adopted with permission from ref. 140. Copyright 2018, American Physical Society.

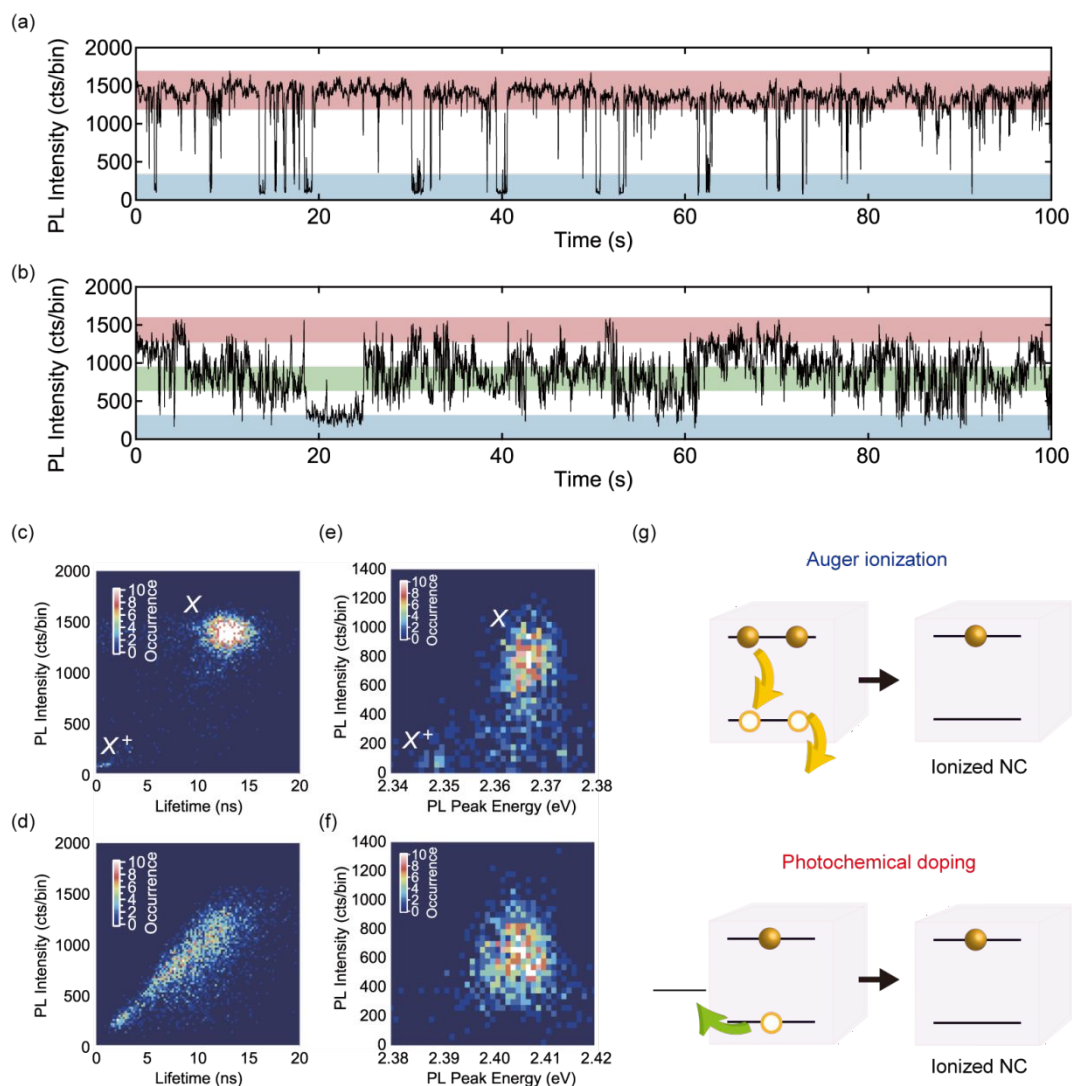


Fig. 7 (a,b) PL intensity time traces which show type A (a) and type B (b) blinking, obtained from single FAPbBr₃ nanocrystals. (c,d) Correlation between PL intensity and lifetime for type A (c) and type B (d) blinking. (e,f) Correlation between PL intensity and PL peak energy for type A (e) and type B (f) blinking. (g) Illustration of two mechanisms for formation of ionized nanocrystals. When the ionized nanocrystals are photoexcited, trion is formed. Panels (a), (b), (d), and (f) are adopted and panels (c) and (e) are reproduced with permission from ref. 141. Copyright 2017, American Chemical Society.

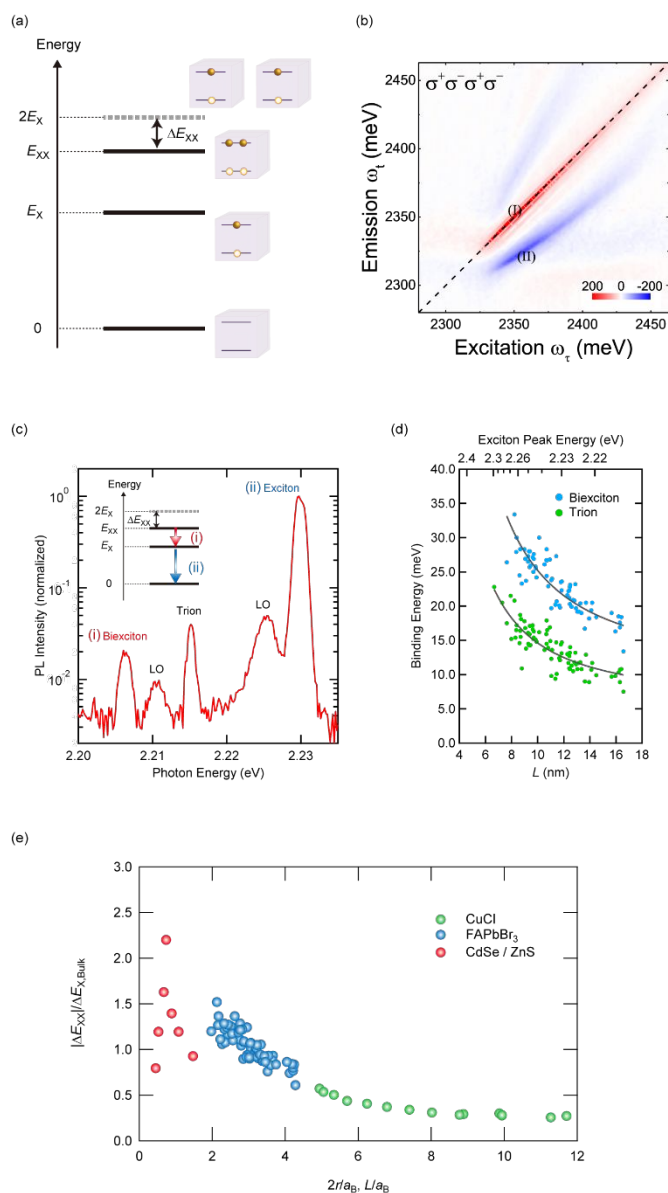


Fig. 8 (a) Energy level diagram of exciton and biexciton states. ΔE_{XX} is the biexciton binding energy. (b) Two-dimensional spectrum of CsPbBr₃ nanocrystals measured by polarization-dependent two-dimensional spectroscopy at 10 K with the cross-circular excitations. The energy difference between the red (I) and blue (II) lines at an excitation energy corresponds to ΔE_{XX} . (c) PL spectrum of a single FAPbBr₃ nanocrystal at 5.5 K. Five PL peaks correspond to exciton, trion, and biexciton PL and two LO phonon replicas. The PL intensity is shown in log scale. The inset shows the optical transitions related to exciton and biexciton PL. (d) Size dependence of the binding energies of biexcitons (ΔE_{XX}) and trions (ΔE_{X^+}). The solid curves are fits using a function of ΔE_{XX} (X^+) = $A/L^2 + B/L + C$. (e) Size dependence of biexciton binding energy in inorganic semiconductor nanocrystals, where the binding energy and the size are normalized by the bulk exciton binding energy and the exciton Bohr radius, respectively. Data are taken from refs. 131, 134, and 164. Panel (b) is adopted with permission from ref. 73. Copyright 2020, American Chemical Society. Panels (c) and (d) are reproduced with permission from ref. 134. Copyright 2021, American Chemical Society.

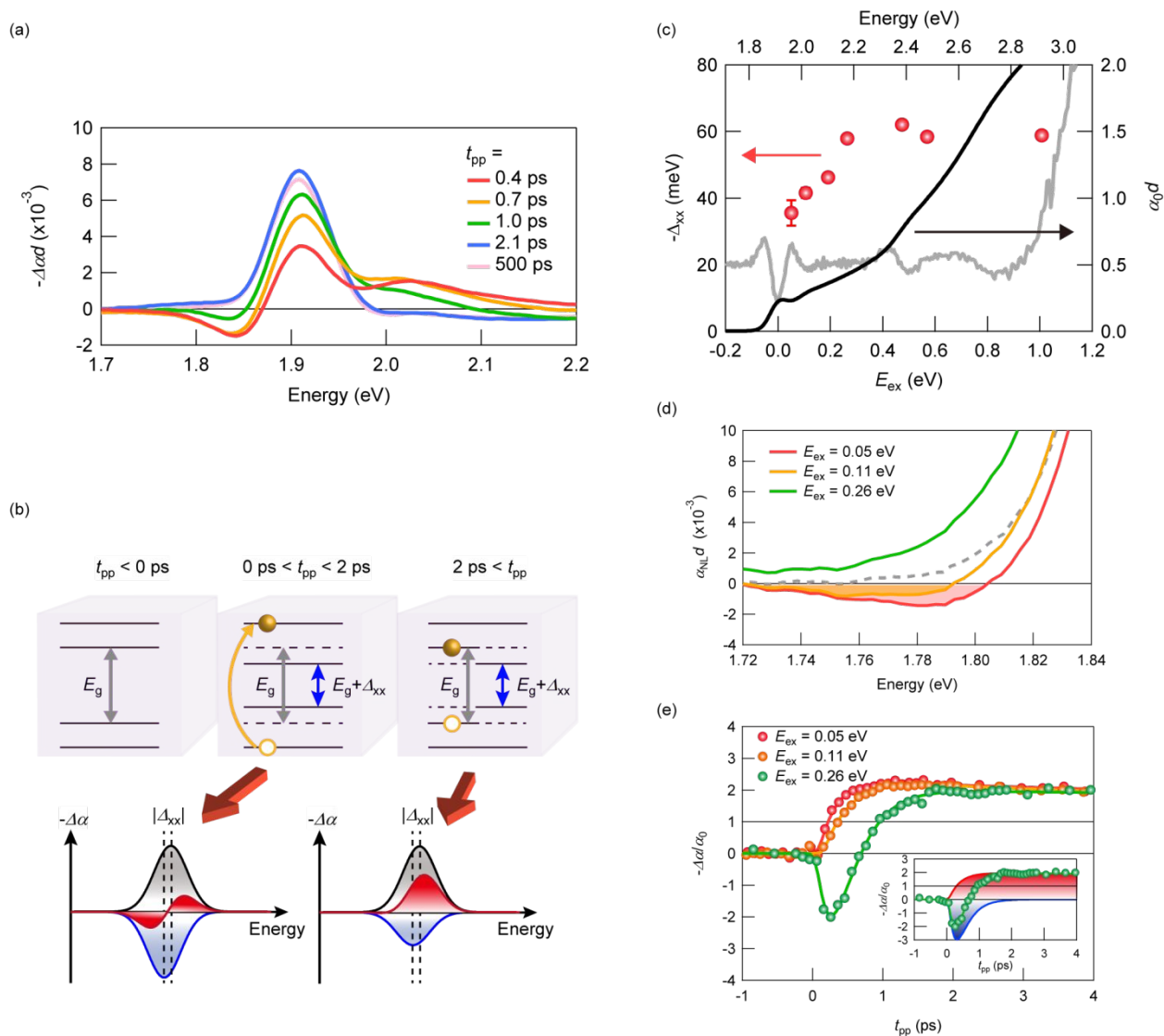


Fig. 9 (a) Change in the absorption spectrum $-\Delta ad$ of CsPbI₃ nanocrystals at different pump-probe delay times t_{pp} for $\langle N \rangle = 0.1$ and the excess energy E_{ex} of 0.47 eV. (b) Schematics of how the biexciton effect modifies the spectra of $-\Delta ad$ at different delay times. The black and blue shaded areas represent the absorption bleaching (centered at E_g) and induced absorption (centered at $E_g + \Delta_{xx}$) signals, respectively. The spectral shape of $-\Delta ad$ is determined by the sum of the two spectra (red shaded areas), which shows a derivative-like feature at $0 \text{ ps} < t_{pp} < 2 \text{ ps}$. (c) Excess energy dependence of the exciton–exciton interaction energy (red dots). The top axis shows the corresponding pump photon energy. The black and gray curves are steady-state absorption spectrum and its second derivative, respectively. (d) Nonlinear absorption spectra at $t_{pp} = 0.3 \text{ ps}$ for three different pump excess energies $E_{ex} = 0.05, 0.11,$ and 0.26 eV , where $\langle N \rangle = 1$. The gray dashed curve is the steady-state absorption spectrum. The shaded spectral region corresponds to the optical gain region. (e) Dynamics of the normalized change in the absorption spectrum probed at 1.80 eV for $E_{ex} = 0.05, 0.11,$ and 0.26 eV and $\langle N \rangle = 1$. The inset shows the induced absorption (blue curve) and bleaching (red curve) components obtained from the fit to the pump-induced dynamics for $E_{ex} = 0.26 \text{ eV}$. All panels are adopted with permission from ref. 70. Copyright 2018, American Chemical Society.

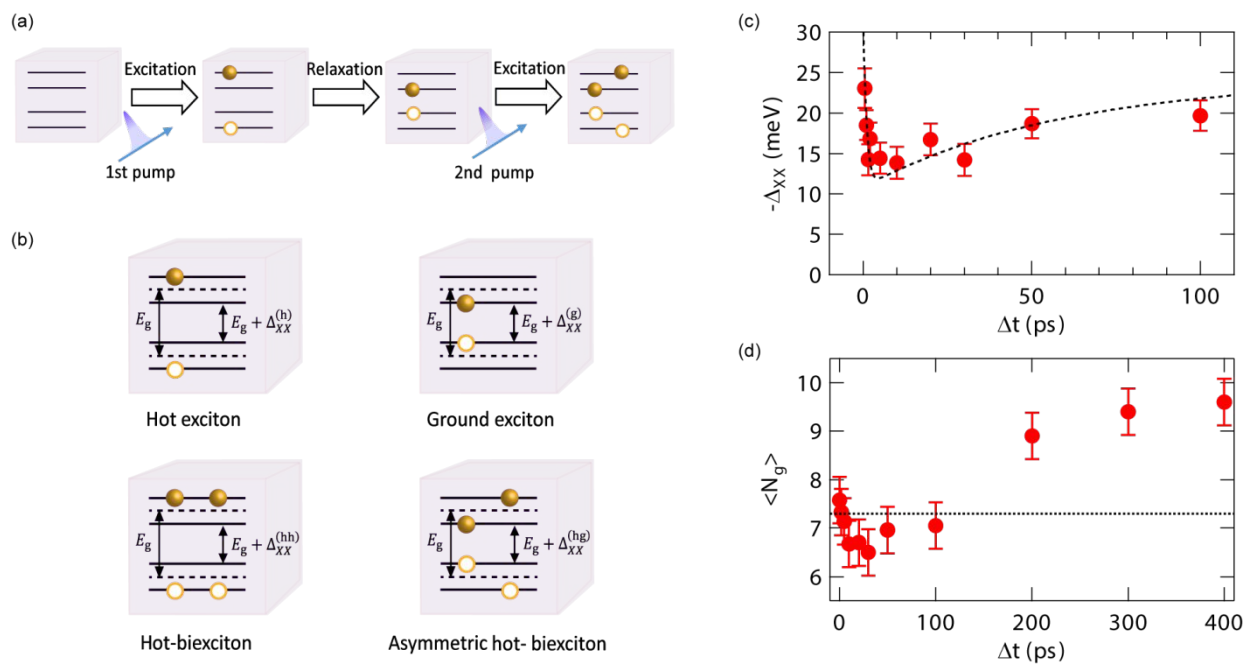


Fig. 10 (a) Illustration of carrier excitation and relaxation dynamics under double-pump photoexcitation. (b) Photoexcited states in lead halide perovskite nanocrystals. E_g is the energy of the lowest energy state of a single exciton. Δ represents the energy shifts induced by exciton–exciton interactions. The superscript h (g) shows that the pump-induced state is one hot (ground) exciton. (c) Pump-pulse interval dependence of the band-edge exciton energy shift for a fixed probe delay time of 0.1 ps in CsPbI₃ nanocrystals. The dotted curve is the fitting result. (d) Pump-pulse interval dependence of the optical gain threshold. The dotted line is the threshold observed from single-pump measurements. Panels (a) and (b) are reproduced and panels (c) and (d) are adopted with permission from ref. 74. Copyright 2020, American Chemical Society.